Applications of Atomic Force Microscopy and Nanopore Translocation in Nanoscale

Microbial Surface and Single Molecules Studies

by

Jiawei Liu

A Dissertation Presented in Partial Fulfillment
of the Requirements for the Degree
Doctor of Philosophy

Approved April 2022 by the
Graduate Supervisory Committee:

Robert Ros, Chair
Stuart Lindsay
Xu Wang
Rizal Hariadi

ARIZONA STATE UNIVERSITY

May 2022

ABSTRACT

To understand the mechanism behind real-life phenomena, e.g., bacterial infection, metabolic disorders and cancer, it is becoming more and more necessary to get to the level of individual cells and single molecules. This dissertation focuses on the application of atomic force microscopy and nanopore translocation related techniques to study microbial surface characteristics and single molecule properties at the nanoscale. At the cellular level, surface characteristics of single wild type and *phoP* mutant *Salmonella typhimurium* cells were analyzed to get a better understanding about the resistance of *Salmonella typhimurium* to antibiotics. These bacteria were grown under different Mg^{2+} concentrations. Mg^{2+} is known to modulate the activities of *phoP* gene which regulates surface structure modifications of *Salmonella typhimurium*. Wild type *Salmonella typhimurium* surfaces were found to have an average roughness of 6.6 ± 0.9 nm for high Mg^{2+} and 6.0 ± 1.3 nm for low Mg^{2+} concentrations, rougher than the 5.3 ± 1.1 nm (high Mg^{2+}) and 5.6 ± 1.5 nm (low Mg^{2+}) for *phoP* mutant. In addition, mutant *Salmonella typhimurium* have average surface potentials of -40 $\pm$ 19 mV (high Mg^{2+}) and 20 $\pm$ 33 mV (low Mg^{2+}), comparing to the -65 $\pm$ 23 mV (high Mg^{2+}) and -71 $\pm$ 27 mV (low Mg^{2+}) of wild-type bacteria. These significant surface characteristics differences will provide insights in the important role of the *phoP* gene in regulating *Salmonella typhimurium* surface structures. On the single-molecule level, the forming components of chromatin from two esophagus cell lines, one normal (EPC2) and one cancerous (CPD), were studied using atomic force microscopy (AFM) recognition imaging. Both EPC2 and CPD chromatin samples were found to contain histone H3 and SMC2, a subunit of the condensin complex. Western blotting results supported this conclusion. Further, DNA translocation speeds through a

nanopore were controlled by utilizing rolling circle replication (RCR) with Φ29 polymerases. This is a major part for future sequencing single glycosaminoglycan (GAG) molecules to resolve their structures. Translocation time on the scale of seconds, which is much longer compared to the translocation of free DNA molecules, had been detected, indicating that the polymerase successfully controlled the translocation process.

DEDICATION

To my parents and sister for their unconditional support

ACKNOWLEDGMENTS

TABLE OF CONTENTS

LIST OF FIGURES

CHAPTER 1

INTRODUCTION

Modern life science is an interdisciplinary field. It combines elements from biology, physics and chemistry. Getting a complete understanding of biological processes is a challenging project. It covers a large amount of length and time scales from organisms, tissues to living cells and single molecules, and from years to milliseconds [1-4]. Although classical ensemble experiments and theories have been contributing significantly to shedding light on the average states of different systems, the underlying mechanisms behind these average behaviors must be fully understood at the level of single cells and single molecules [1-6]. My research focuses on applying atomic force microscopy (AFM) and nanopore translocation related techniques to understand the characteristics of single cells and single molecules at the nanoscale levels. Since the development of AFM in 1980s, it has been emerged as a powerful tool to analyze the morphological, mechanical and electrical characteristics of various biological samples such as biomolecules, biopolymers, biological membranes, fibers, and cells either in a controlled atmosphere or in a liquid environment [7-13]. Nanopore translocation technique has been introduced in the mid 1990's. It allows to detect the presence of biomolecules by the observations of measurable changes in the ion currents through nanopores. Through nearly three decades, numerous milestones were accomplished with it, e.g., the distinguishment of purine and pyrimidine segments in single RNA molecules, single-nucleobase discrimination among nucleobases in a DNA strand, detection of single molecules of DN. Further. nanopores are taking the center stage as a tool that promised to read a DNA sequence [14-19].

1

For my Ph.D, the first biological system analyzed using AFM related techniques is *Salmonella typhimurium*. *Salmonella typhimurium* is a typical Gram-negative bacterium. Gram-negative bacteria can cause infections including pneumonia, bloodstream infections, surgical site infections and meningitis [20-22]. And in 2018, a *Salmonella typhimurium* outbreak spread to 8 states, infected at least 265 people with one person being killed according to Centers for Disease Control and Prevention. Gram-negative bacteria can be resistant to various drugs and are increasingly resistant to most available antibiotics. One important factor behind the drug resistance of Gram-negative bacteria is their cell surface structures. I characterized the surfaces roughness and surface potential of the virulent Gram-negative bacteria *Salmonella typhimurium* and a non-virulent mutant on the single bacteria level. The results will be explained in Chapter 3. The second biological system studied is chromatin extractions from normal esophageal cells (EPC2) and cancerous esophageal cells (CPD). And in order to characterize chromatin structure variations for EPC2 and CPD, we used atomic force microscopy recognition imaging at the single molecule level. We identified histones H3 and chromosome maintenance protein SMC2 in both native human chromatin extractions. This demonstrates the capability of AFM recognition imaging of analyzing the components of the chromatin in human cell extractions. This part will be covered in Chapter 4 of this dissertation. Lastly, a method of controlling the translocation speed of glycosaminoglycan (GAG) molecules through solid-state nanopores for sequencing of single GAG molecules using recognition tunneling technique was developed. Sequencing GAG molecules is an unsolved problem. Recognition tunneling in nanopore translocation experiments has been demonstrated to be a powerful tool for DNA sequencing. For GAG, the idea is to utilize the same approach.

2

However, the timescale of translocation of free GAGs through the nanopore is about 90 μs [23]. This translocation speed is too fast for proper recognition tunneling data collection. Controlling the translocation speed of GAGs is therefore a major barrier to successfully sequence GAGs. GAGs can be conjugated to DNA. The translocation speed of GAGs can be controlled through the controlling translocation of DNA molecules. We demonstrated that the translocation of DNA through solid-state nanopores can be controlled by $\Phi 29$ DNA polymerases. Seconds long translocation events were observed in our experiments. With this, GAG recognition tunneling sequencing should be possible. Chapter 5 is dedicated to this project. In addition, Chapter 2 covers the biological background and the techniques used in my research.

CHAPTER 2

BACKGROUND

2.1 Gram-negative Bacteria

Gram-negative is a term that originates from the Gram stain method. In the Gram stain method, the bacteria will be first stained with violet-iodine complex and some counterstain, commonly safranin or fuchsine. Then the stained bacteria can be treated with alcohol. Stained Gram-negative bacteria will decolorize under this treatment [24, 25]. Gram-negative bacteria include the model bacteria *Escherichia coli* and many pathogenic bacteria, like *Pseudomonas aeruginosa*, *Chlamydia trachomatis*, *Yersinia pestis* and *Salmonella typhimurium*.

The cell envelope of Gram-negative bacteria has multiple layers. It is consisting of two distinct membranes, the cytoplasmic or inner membrane (IM) and the asymmetric outer membrane (OM). The IM is a standard phospholipid bilayer. OM contains phospholipids in the inner leaflet and lipopolysaccharides (LPS) in the outer leaflet [26-28]. As Gram-negative bacteria have two membranes, they are defined as "diderm" bacteria [29]. The Gram-negative bacteria cell envelope and LPS structure can be seen in Fig 2-1 [28]. LPS are large amphipathic glycoconjugates that are composed of a hydrophobic lipid domain (Lipid A), the repeating hydrophilic distal oligosaccharide (O-antigen), and the hydrophilic core polysaccharide. Among these three components, Lipid A is an endotoxin and the main virulence factor [26].
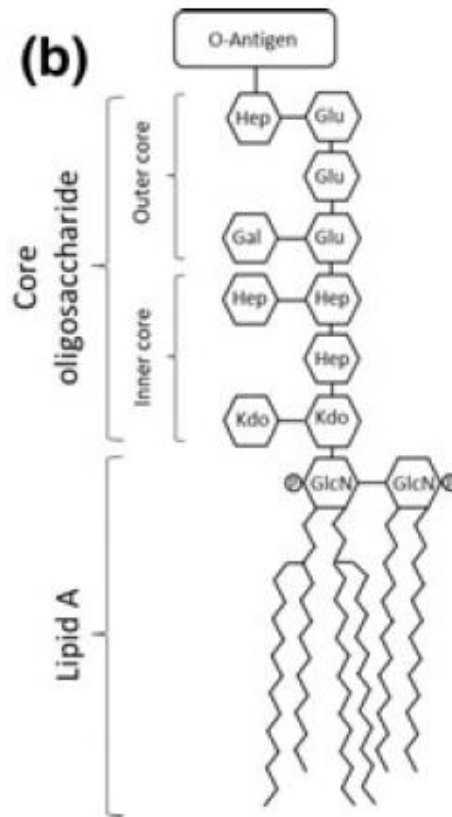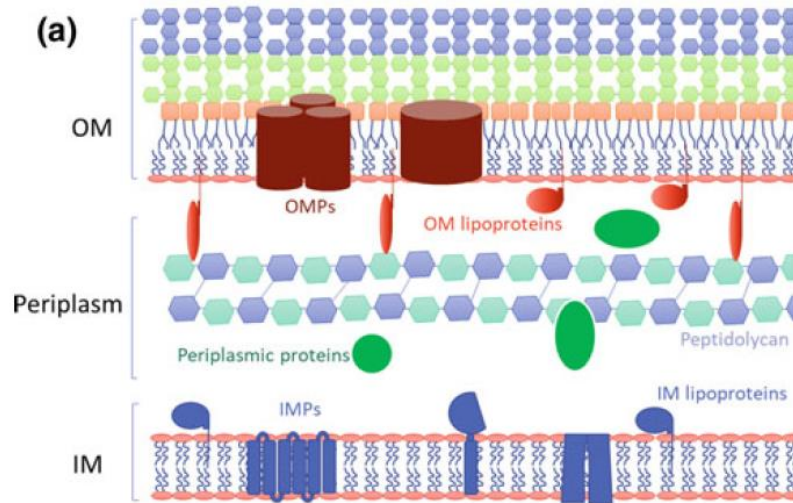
Fig 2-1. The Gram-negative bacteria cell envelope and lipopolysaccharide structure.

(a) Architecture of the Gram-negative bacteria cell envelope. IM and OM are separated by

an aqueous periplasm which contains the peptidoglycan cell wall. Major membrane proteins are shown in different colors: Inner membrane proteins (IMP) and IM lipoproteins in blue; outer membrane proteins (OMP) in brown; OM lipoproteins in orange. Soluble proteins in the periplasm are colored green. (b) Illustration of the structure of lipopolysaccharide (LPS). The hydrophobic Lipid A is attached to a core oligosaccharide and then the distal O-antigen. Both images are adapted from [28].

2.2 Atomic Force Microscopy

Atomic force microscopy (AFM) was developed by Binnig, Quate, and Gerber in the 1980s [30]. It is the most widely used technique in the scanning probe microscopy (SPM) family. Since its invention, AFM has been used for single molecular study and surface analyses. Importantly, AFM can be operated in aqueous environments and at physiological temperatures. AFM can trace the topography of biological samples without the need for chemical fixation or labeling [8, 30]. And it is quickly recognized that AFM can characterize and design biological systems [31].

Further, using conductive AFM probes, the electronic properties of biological materials can be studied [32-34]. Below, the working principles, standard operations modes together with some advanced applications of AFM are introduced.

2.2.1 AFM Working Principles

A simplified diagram for AFM is shown in Fig 2-2 (a) [9]. A piezo-controlled cantilever can approach and retract from the sample surfaces. When the tip comes close to the sample

surface, it feels a verity of forces form the sample, including van der Waals forces, dipole-dipole interactions, electrostatic forces, repulsive forces. The resulting force will cause the bending or oscillation changes of the cantilever, which will result in a change of the signal of the reflected beam on the photodiode detector. Through the position variations of the reflected beam on the photodiode detector, the characteristics of the sample can be extracted with related electronic feedback loops. AFM can be used for both detecting and manipulating single molecules.
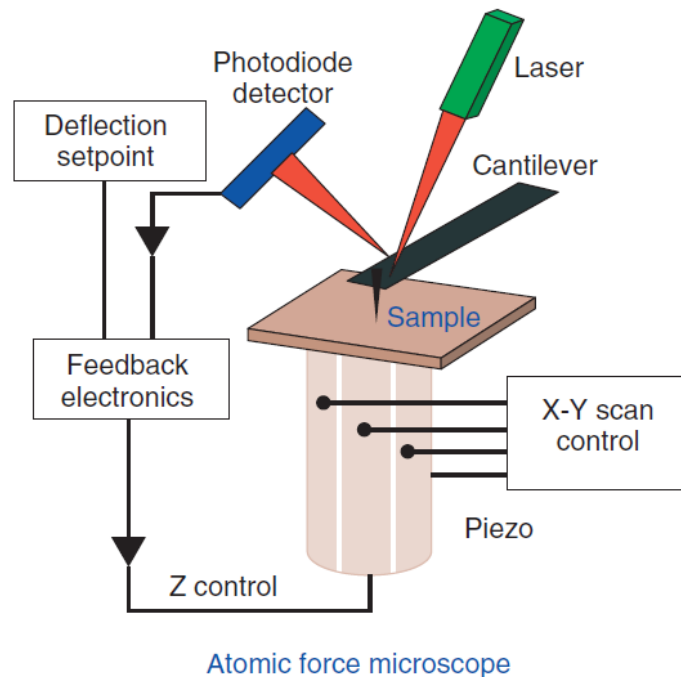
Fig 2-2. Schematic of an atomic force microscopy. A sharp tip at the end of a microcantilever is brought close to a prepared sample. As the sample is scanned over, the interaction between the sample and the tip will bend the microcantilever which will change the position of the reflected laser on the photodiode. Feedback electronics will provide

some voltage signal to maintain the position of the reflected laser. Surface topological information can be derived from this feedback signal. The image is adapted from [9].

2.2.2 Standard Operation Modes of AFM

AFM can be mainly operated in three modes: contact mode, non-contact mode and tapping mode. A typical force-displacement curve between the tip and the sample surface is shown in Fig 2-3 [7].
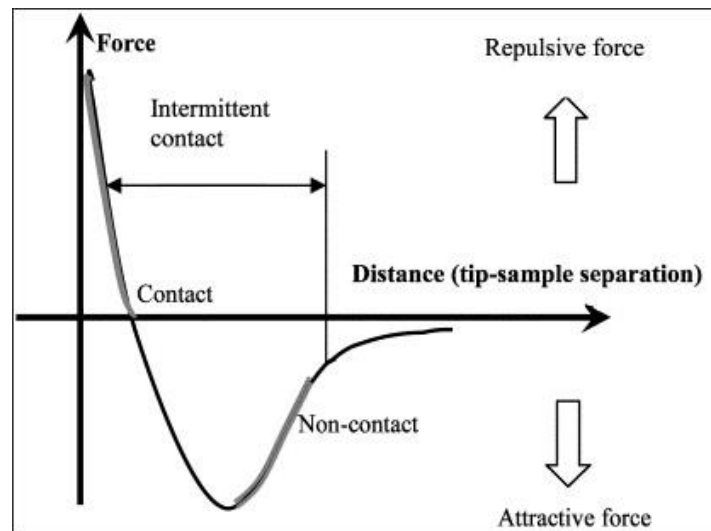
Fig 2-3. Interatomic force variation versus distance between AFM tip and sample. When AFM tip is far away from the surface, weak attractive forces are generated between the AFM tip and the sample. As the AFM tip approaches the sample closer, the attractive forces increase first and then decrease when the electron clouds begin to repel each other electrostatically. The attractive forces weaken more as the distance between the AFM tip and the sample decreases more. The interaction force becomes zero when the distance

between the AFM tip and the sample reaches a couple of angstroms. After the AFM tip is in contact with the sample, the interaction force will become fully repulsive. The figure is adapted from [7].

In contact mode, the cantilever tip is in close contact with the sample surface and the cantilever tip drags over the surface in physical contact. The cantilever will be bent because of the repulsive force from the sample during the imaging process. Due to the close contact between the cantilever tip and the sample surface, soft samples can be damaged due to the dragging lateral forces exerted by the cantilever tip.

In 1987, Martin et al. pioneered the use of AFM in an oscillating mode. During their experiments, the cantilever was away from the sample surface (5 to 15 nm above the sample surface) and the cantilever was oscillating near its resonance frequency. They adopted very small vibration amplitudes (below 1 nm) for the cantilever tip to connect changes in the oscillation amplitude, phase or frequency with variations in the derivative of the force along the normal to the sample surface. The changes were mainly dominated by long-range attractive forces of van der Waals type. This was called later non-contact mode [7, 35]. A few years later, Zhong et al. introduced some modifications to this. They applied large amplitudes (up to 100 nm) to the cantilever. And they used relatively stiff cantilevers with spring constants of about 40 N/m. The oscillation amplitude reduction was because of short-range repulsive forces. This is the tapping mode [36].

2.2.3 Kelvin Probe Force Microscopy

Kelvin Probe Force Microscopy (KPFM) or Scanning Kelvin Probe Force Microscopy (SKPFM) is a technique to measure the electrical potential difference between AFM probe tips and sample surfaces. For applying KPFM, the AFM probes and substrates need to be conductive. Usually, the curvature of a conductive AFM probe tip is about 25 nm.

After the probe successfully approaches the substrate, the distance between the probe tip and the substrate is smaller comparing to the size of the probe tip curvature. The local area between the tip and substrates can be assumed to form a parallel plate capacitor. During the experiments, an AC electric signal is applied to the conductive probe. Because of the potential difference between the probe and the local surface, the oscillation of the probe under this AC signal is affected, and the DC feedback loop will react to reestablish the preset oscillation characteristics and offset the effect. The DC signal that was used to cancel this effect is related to the local potential difference between the probe and surface. If the probe's potential is calibrated, the local potential of the surface can be obtained. The mechanism for KPFM is shown in Fig 2-4.
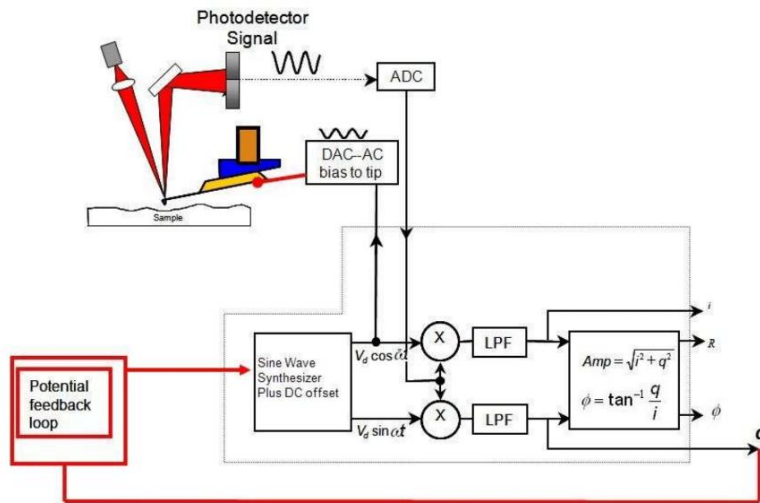
Fig 2-4. Kelvin Probe Force Microscopy. This is adapted from Asylum Research applications guide, version 13.

As the probe and the local surface are modeled as a parallel plate capacitor, when an AC signal is applied to the probe, the force between the two plates is proportional to the square of the applied voltage:

$$F = \frac{1}{2} * \frac{\partial C}{\partial z} * V^2$$

The total potential difference between the probe and the sample is the sum of the applied AC bias (V_{AC}), the potential difference we are trying to measure (V_{CPD}), and any DC voltage we wish to apply (V_{DC})

$$V = V_{DC} - V_{CPD} + V_{AC} \sin \omega t$$

This leads to:

$$V^2 = (V_{DC} - V_{CPD})^2 + 2(V_{DC} - V_{CPD}) V_{AC} \sin \omega t + \frac{1}{2} V_{AC}^2 (1 - \cos 2\omega t)$$

So, $F = \frac{1}{2} * \frac{\partial C}{\partial z} \left\{ \left[(V_{DC} - V_{CPD})^2 + \frac{1}{2} V_{AC}^2 \right] + 2(V_{DC} - V_{CPD}) V_{AC} \sin \omega t - \frac{1}{2} V_{AC}^2 \cos 2\omega t \right\}$

The forces related to the AC signal applied are the ωt and $2\omega t$ terms. However, the probe usually does not interact with the $2\omega t$ during its resonance. The main term to analyze is the middle part of the equation, which is related to the potential difference between the probe and local surface and the DC voltage applied to the probe. To minimize the force applied to the probe because of V_{CPD}, V_{DC} should be equal to V_{CPD} in the above equation. Through this mechanism, we can map the potential difference between the probe and the surface.

In my research, MFP 3D AFM from Asylum Research was used for KPFM. For this type of AFM, a two-pass method called nap mode is adopted. The first pass is used to map the topography of the surface like a standard tapping mode. During the second pass, the probe is raised above the surface for a specific distance Δz to probe the surface potential. The two-pass method is shown in Fig 2-5.
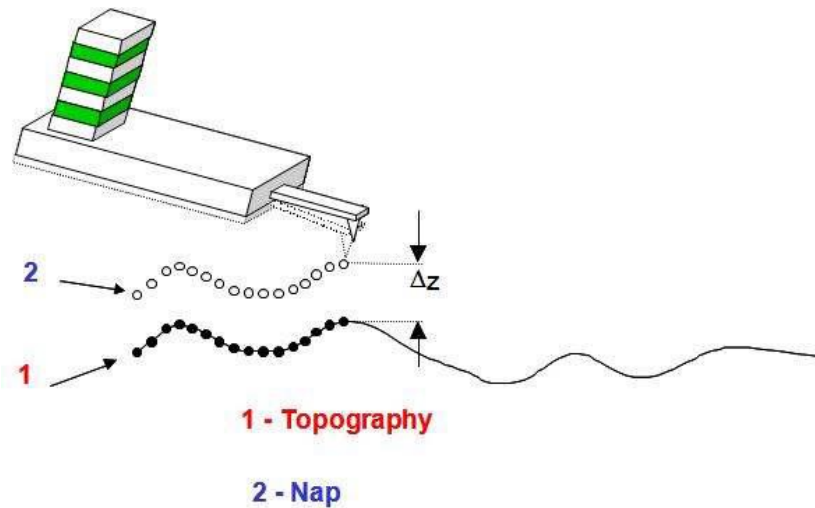
Fig 2-5. Two-pass KPFM. The cantilever was first tuned using a normal tapping mode driven signal so that during the first pass, the cantilever can be operated in tapping mode and image the topography of a surface. During the second pass, the cantilever is lifted above the surface for an appropriate height (a few tens of nanometers). An AC signal was applied to the cantilever directly. The oscillation of the cantilever under this AC signal is affected by the potential difference between the cantilever and the surface. Then a DC signal is applied to the cantilever to offset this effect. Figure is adapted from Asylum Research applications guide, version 13.

2.2.4 AFM Recognition Imaging

AFM recognition imaging is a label-free technique to identify specific molecules from compositionally complex samples while mapping the topography of the samples simultaneously in a liquid environment [37]. It requires a sensitive imaging mode, typically the so-called MAC mode, where the AFM cantilever is driven directly by a magnetic field which will reduce the movement of liquid surrounding the tip and increase signal to noise ratio. The AFM cantilevers used in MAC mode need to have a ferromagnetic coating like nickel in order to be driven by a magnetic field. For recognition imaging, the cantilever is modified with specific antibodies or other recognition molecules (e.g., aptamers) through polyethylene glycol (PEG) linkers and the samples containing corresponding antigens will be immobilized on the substrate. The cantilever is oscillating under a magnetic field. When the tip with the antibodies approaches the substrate, the antibody molecules will bind to antigen molecules on the surface. At this point, the PEG-linker is not stretched. The AFM cantilever is operating in tapping mode. The topography of the sample surface will be obtained. When the cantilever retracts from the surface, the PEG-linker will start stretching. After the cantilever reaches some position, the PEG-linker will be stretched. Because of the binding force between antibodies and antigens, the oscillation amplitude of the cantilever will decrease. The change of the oscillation amplitude will be recorded as the recognition signal which indicates the specific binding between selected antibodies and the prepared sample, as can be seen in Fig 2-6 [38].
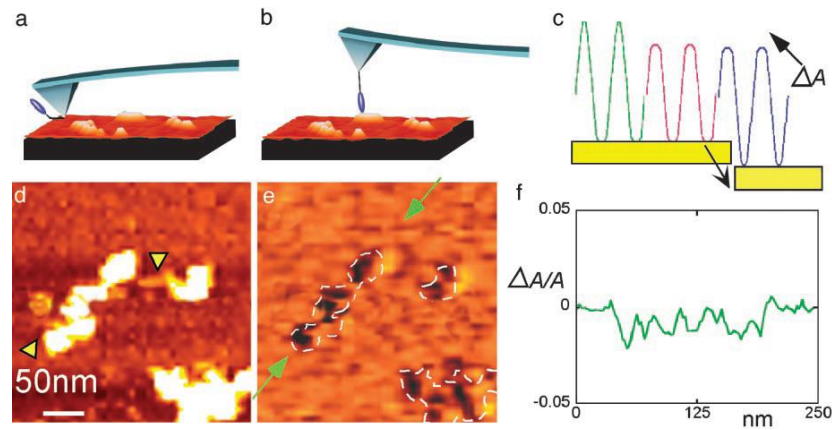
Fig 2-6. Recognition imaging. (a) An AFM cantilever modified with antibodies approaches antigens modified surface. (b) One antibody binds to its antigen and PEG-linker is fully stretched. The cantilever is being pulled by the binding force between the antibody and its antigen. (c) The oscillation amplitude of the cantilever decreases because of the binding force. The imaging servo restores the signal amplitude but with the peak signal shifted downward by an amount ΔA (blue curve in (*c*). This peak shift provides the recognition signal for a specific antigen-antibody recognition event. (d) A topography image shows where mouse mammary tumor virus (MMTV) arrays reside (bright white blobs). (e) Black dots in the related recognition image show that MMTV arrays are recognized. (f) Relative recognition signal comparing to the initial oscillation amplitude of the cantilever is drawn. The highest features in *d* are about 5 nm, adapted from [38].

In 1999, Raab et al. introduced AFM recognition imaging by imaging lysozyme with antibodies functionalized cantilevers [37]. The robust, reliable and well-described avidin-biotin interaction provides an ideal system for AFM recognition imaging. In 2005, Ebner et al. utilized AFM recognition imaging on the pair and analyzed their binding properties

[39]. Since then, AFM recognition imaging has been applied to various biological systems. Wang et al. imaged the human Swi-Snf (hSwi-Snf) nucleosome remodeling complexes using AFM recognition imaging and applied the information about hSwi-Snf to locate hSwi-Snf complexes bound to reconstituted mouse mammary tumor virus (MMTV) promoter nucleosomal arrays [40]. And in 2008, Wang et al. went further by applying AFM recognition imaging on native centromeric chromatin samples from drosophila. They identified centromere-specific histone 3 (CenH3) within histone core particles directly [41].

2.3 Nanopore Translocation

The nanopore technique is introduced in the mid-1990s. The instrumentation consists of two chambers containing electrolytes and separated by a thin membrane with a nanometer-scale pore. When voltages are applied to the two chambers (*cis* and *trans*), electrolytes will move under the electric field, resulting in an ion current [16]. A nanopore can be viewed as a nanofluidic channel for the transport of charged molecules. For example, when nucleic acid molecules are driven through a nanopore by the electric field, their structure features can be identified through the change of the trans-membrane ion current. This is the fundamental mechanism for DNA sequencing using nanopores. Back in the late 1940s, Wallace H. Coulter developed orifice-based resistive counters to count blood cells. This technique was patented in 1953 [42]. In the 1970s, DeBlois and Bean were able to refine Coulter's hole-based technique to detect nanoscale particles and viruses using sub-micrometer trach-etched pores [43]. This propelled the birth of the nanopore technique. However, a significant push for the invention of the nanopore technique is intimately related to ion-channel electrophysiology which is used to monitor protein ion channel

15

dynamics in synthetic planar lipid bilayer geometries. There are mainly two types of nanopores: biological nanopores and solid-state nanopores. One main type of biological nanopores is toxin α-hemolysin secreted by *Staphylococcus aureus* [16, 44], shown in Fig 2-7 a. It propelled the fast progress of nanopore-based biomolecular analysis. However, comparing to the size of one single DNA base, the channel of α-hemolysin is too long. This increases the complexity of resolving translocation signals of single nucleotides, which will hinder DNA sequencing. Another type of biological nanopore, MspA from *Myobacterium smegmatis* was engineered to solve this problem [16, 45], shown in Fig 2-7 b. Its inner constriction length is about 1 nm. This improves the discrimination of different DNA bases. Other biological systems like modified phi29 viral packaging motors and engineered DNA origami can be used for nanopore experimentation as well [16, 46], shown in Fig 2-7 c. Because of the considerably small channel length of biological nanopores, the noise level is low, usually a few tens of pico-Amperes. However, biological nanopores cannot be stored long, and they have high requirements for the physiological conditions they are used in. Instead, solid-state nanopores generally have a noise level above 100 pA, have a long lifetime. They can also be easily reproduced and can tolerate various environmental conditions. Solid-state nanopores are usually fabricated on synthesized membranes like silicon nitride, aluminum oxide, boron nitride or hafnium oxide. In our case, we used silicon nitride membrane with a thin layer of silicon dioxide on top to produce the nanopores. The images of a solid-state nanopore and schematic of a simplified solid-state membrane nanopore setup are shown in Fig 2-8.
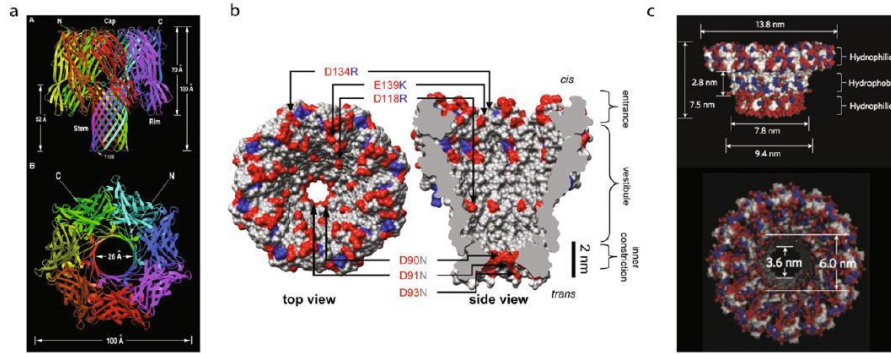
Fig 2-7. Examples of biological nanopores. (a) The toxin α-hemolysin secreted by *Staphylococcus aureus* [44]. (b) MspA from *Mycobacterium smegmatis* [45]. (c) Engineered phi29 viral packaging motor [46].
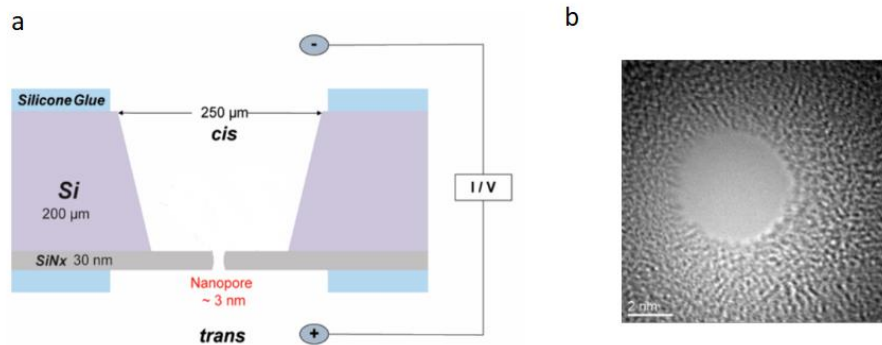
Fig 2-8. Examples of a solid-state membrane and a solid-state nanopore. (a) Schematic of a solid-state silicon nitride membrane supported by silicon base and simplified nanopore experiment set up are included, where cis represents the bottom chamber and trans represents the top chamber. The chip was glued onto the cis chamber using silicon glue. The figure is adapted from [23]. (b) A solid-state nanopore drilled by electron beam.

17

During nanopore translocation experiments, the nanopore will be confined between two chambers. The two chambers usually will be filled with solutions that contain KCl because of the small sizes of K^+ ions. The concentration of KCl depends on the requirements of the experiments. When the nanopore translocation experiments start, the voltage will be applied across the nanopore membrane through non-polarizable Ag/AgCl electrodes. Two reversible electrochemical reactions will take place at the electrodes. An oxidative electrochemical reaction Ag(s) + Cl$^-$ → AgCl(s) + e$^-$ occurs at the anode (+). Cl$^-$ was captured from the solution at the electrode. An electron migrates through the wire to the electrometer, producing current and generating a charge imbalance at the electrode. This results in cation migration towards the membrane (typically K$^+$ or Na$^+$ ion). At the cathode, reaction AgCl(s) + e$^-$ → Ag(s) + Cl$^-$ occurs. The released chloride ion will migrate towards the membrane and an electron will be used from the circuit [16]. According to [47], in the bias window ($\pm$ 1 V vs. Ag/AgCl for aq. KCl), the above reverse reaction will be the sole reaction that occurs. The current-voltage response for a nanopore is Ohmic. If the bias values are increased more, non-linear electrochemical processes and pH instability will occur. For this reason and other reasons (e.g., membrane instability), nanopore experiments are frequently performed under biases lower than 1 V.

The basics of nanopore measurements are shown in Fig 2-9. The nanopore experiment schematic is a simplified version of Fig 2-8. Fig 2-9 shows a pore in a generic membrane of arbitrary dimensions, the electrochemical half-cells on either side of the membrane, and the current measuring device. When the voltage is within the linear bias window, a steady constant DC current will be produced. This serves as the baseline current signal. When

18

individual macromolecules enter and exit the nanopore, resistive pulses will be produced. This is because the flow of ions will be partially blocked by the presence of macromolecules in the nanopore. The dwell time of the molecule in the pore (t_d) will be the duration of a pulse signal. And the amplitude of a pulse signal δI will be related to the size of the macromolecule for the same nanopore. In addition, the diffusion of macromolecules is a stochastic process. The waiting time between two successive pulse events (δt) varies over time. Respectively, these parameters report on a biopolymer's length and its interactions with the pore, its cross-sectional diameter and its solution concentration [16].
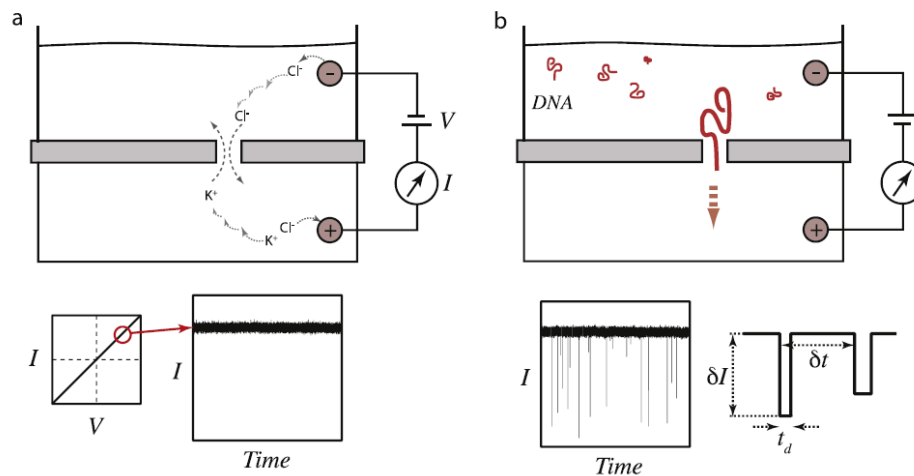
Fig 2-9. The basics of nanopore measurements. (a) During the linear bias window, when voltage is applied across the nanopore, the reverse electrochemical reaction will cause the migration of ions to the membrane. Transport of the ions across the nanopore will lead to electric current which can be measured by a high-bandwidth electrometer. It is a steady-state DC current signal. (b) shows how a pulse signal is related to the presence of a macromolecule in the nanopore, adapted from [16].

When the voltage V is applied across a cylindrical pore with a diameter d and length h, the ion current I_o through the pore is approximated in high ionic strength solutions (> 100 mM) by:

$$I_o = V(e[n_+\mu_+ + n_-\mu_-]) \left(\frac{4h}{\pi d^2} + \frac{1}{d}\right)^{-1} + V\mu_C \frac{\pi d}{h} \sigma$$

where n is the number density of the species in the electrolyte, μ is their respective electrophoretic mobility [16]. With KCl solution as the electrolyte, the first term can be simplified into $(\mu_K + \mu_{Cl})n_{KCl}$. The first term was explained in early works of nanopore studies [48, 49]. The second term represents conductance. For thicker pores, the conductance scales with d^2. For thinner pores, the conductance scales linearly with d. The last term is related to electroosmotic flow. This is caused by the surface charge of the nanopore. σ is the surface charge density. μ_C is the mobility of the counterion which screens the surface charge [50].

2.4 Chromatin Structures

For eukaryotic cells, the genes that store heredity information are present in the format of chromosomes in the small nucleus. Chromosomes are formed by chromatin. The fundamental units of chromatin are nucleosomes. The crystal structure of one nucleosome is shown in Fig 2-10. Nucleosomes consist of histones and DNA, specifically of two H2A and H2B dimers and one H3-H4 tetramer. The histones form an octameric complex with DNA wrapping around it. This is the core of one nucleosome [51]. These nucleosome cores will further assemble into chromatin fibers and subsequently chromosomes through linker

histone H1 and linker DNA [52, 53]. Different levels of DNA organization within chromatin structure are shown in Fig 2-11.
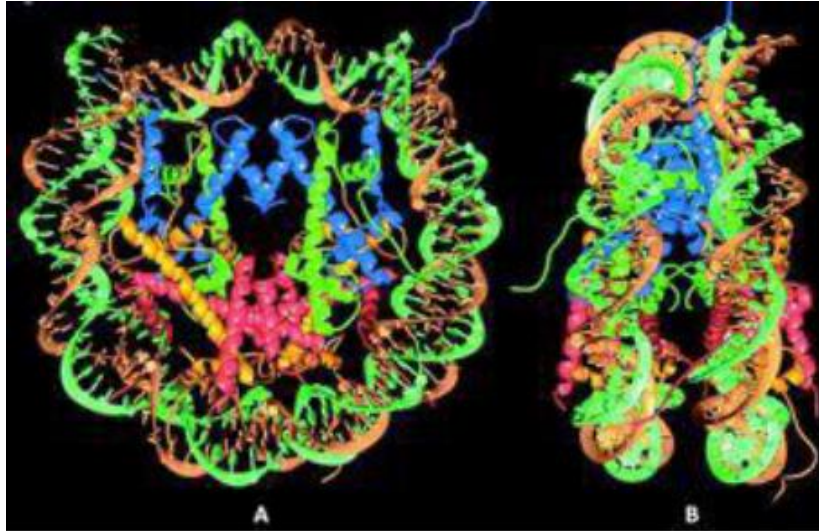
Fig 2-10. Crystal structure of one nucleosome. (A) Crystal structures of one nucleosome consisting of H2A, H2B, H3, H4 and DNA wrapped around them. (B) Perpendicular view of the crystal structure, adapted from [51].
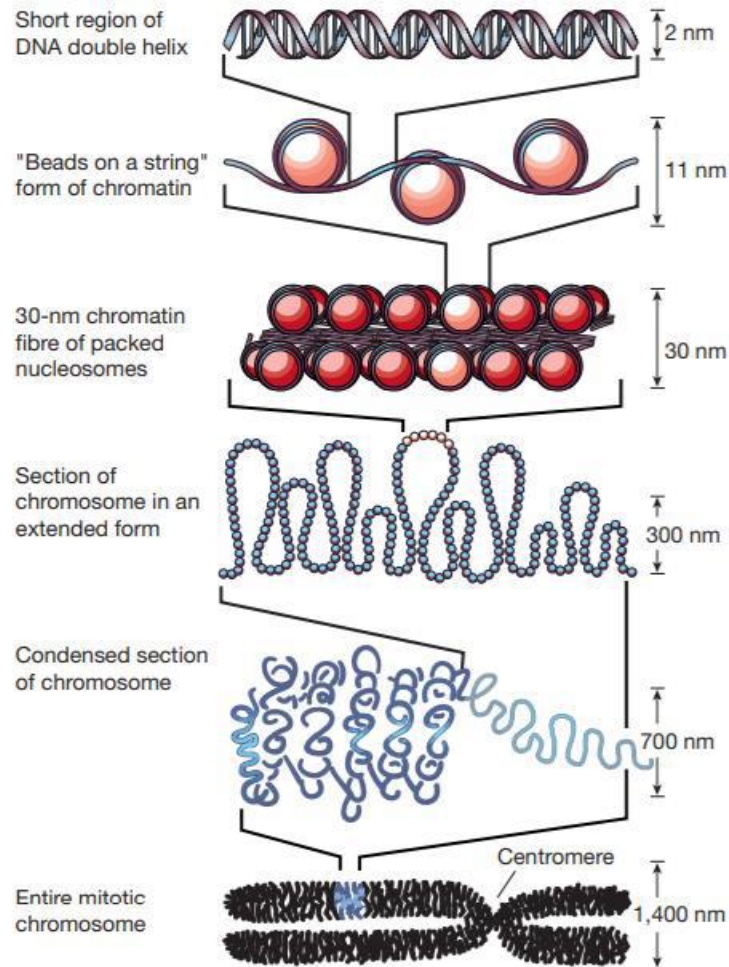
Fig 2-11. The organization of DNA within the chromatin structure. The lowest level of organization is the nucleosome, in which two super helical turns of DNA (a total of 165 base pairs) are wound around the outside of a histone octamer. Nucleosomes are connected by short stretches of linker DNA. At the next level of organization, the string of nucleosomes is folded into a fiber of about 30 nm in diameter, and these fibers are then further folded into higher-order structures. At levels of structure beyond the nucleosome, the details of folding are still uncertain, adapted from [54].

It has been shown that the transcription, replication and DNA damage repair are all closely related to the chromosome conformation in the nucleus [55]. Many experiments have been done about the nuclear organization by fluorescence in situ hybridization (FISH) [56, 57] before sequence-specific chromatin structure was analyzed by chromosome conformation capture (3C) [58] related techniques, like circular chromosome conformation capture (4C) [59], chromosome conformation capture carbon copy (5C) [60] and high-resolution 3C (Hi-C) [61]. These techniques illustrate the relationship between chromosome structure and nuclear biology in a quantitative way. In the 3C technique, the chromatin is cross-linked first in the nucleus and digested by restriction enzymes. The digested chromatin would go through an intramolecular ligation at a very low DNA concentration. After ligation, cross-linking of chromatin was reversed and the formation of hybrid DNA can be quantified by polymerase chain reaction (PCR) using locus-specific primers [56, 58]. The process is shown in Fig 2-12 (A). Through many experiments, complex chromosome structural patterns can be revealed. At large scale (tens of megabases), genomic sequences tend to fall into A and B compartments which might be related to the phase transition of chromatin-associated proteins. The two compartments are characterized by the spatial segregation of open and closed chromatin. With the aid of the labels (A and B), the regions on different chromosomes that have correlated contact profiles and anticorrelated contact profiles can be identified. The regions tend to be closer in space if they belong to the same compartment (A vs. B) than if they do not. At a shorter scale (< 1 Mb), chromosome forms topologically associating domains (TADs) [55]. These patterns can be seen in Fig 2-12 (B). TADs are domains whose boundaries are most conserved during cell differentiation according to Zhan et al. even though they cannot be defined exactly due to complex sub-

megabase interaction patterns [62]. At even sub-TAD scale, DNA-binding factor CTCF-related point interactions and stripes are common as shown in Fig 2-12 (B) [63-65]. Even though the 3C related techniques have been productive in analyzing the chromosome structures, there are a few drawbacks that are related to the procedures of these methods. First, contacts by indirect cross-linking events through intervening nuclear proteins or even organelles can be formed during cross-linking. And second, non-specific molecular hybrids between crosslinked and partially solubilized chromatin can appear during ligation. The invention and development of AFM recognition imaging in the late 1990s and early 2000s however provides a new way to simultaneously measure the topography and the local nanoscale structures of chromatin instead. Wang et al. conducted single epitope AFM recognition imaging on native Drosophila chromatin [41]. Lin et al. in 2009 analyzed the acetylation of chromatin using DNA aptamer through AFM recognition imaging [66]. In my research, we utilized AFM recognition imaging to analyze the forming components of native chromatin from normal (EPC2) and cancerous (CPD) esophageal cell lines.
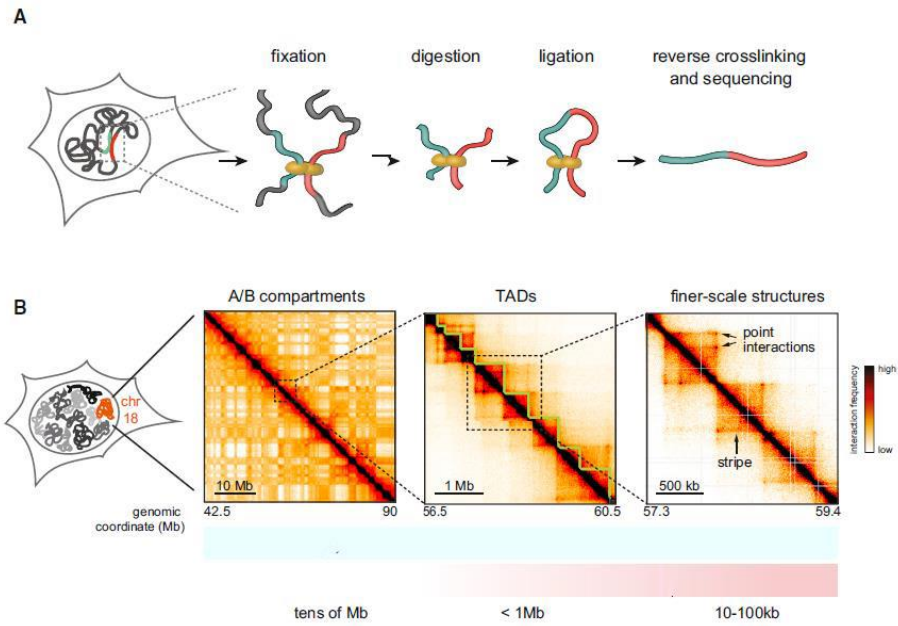
Fig 2-12. 3C method and different scale chromosome conformations. (A) Scheme of the core steps in chromosome conformation capture (3C) methods. (B) The folding of mammalian chromosomes into checkerboard-like A/B compartments (left), TADs (middle), and shorter-scale structures (right). Sub-TAD structures include CTCF-related point interactions and stripes (arrows), adapted from [55].

CHAPTER 3

ROUGHNESS AND SURFACE POTENTIAL DISTRIBUTIONS OF SALMONELLA

TYPHIMURIUM

3.1 Introduction

Gram-negative bacteria can cause numerous infections, such as pneumonia, bloodstream infections, wound or surgical site infections and meningitis in healthcare settings. The outer membrane (OM) of Gram-negative serves as a selective permeation barrier which prevents the passive diffusion of many solutes such as antibiotics and detergents into the cell [67, 68]. Lipopolysaccharides (LPS) are the major component of the OM. LPS is a highly acylated saccharolipid and plays an important role in maintaining the barrier function of OM. The hydrophobic lipid A moiety helps to block the flux of hydrophilic molecules through the OM. The hydrophilic O-antigen offers a barrier against the transport of hydrophobic compounds. And the aliphatic domain which is made of fully saturated fatty acyl chains creates a gel-like lipid interior. This contributes to the low permeability of hydrophobic solutes across the OM. Overall, the presence and the peculiar arrangement of LPS allows Gram-bacteria cells to survive in harsh environments [28, 68-70]. And due to the structure of LPS, it increases the negative charge of the cell membrane.

LPS is a polyanionic molecule. The inner core oligosaccharide part of LPS contains 3-deoxy-D-manno-octulosonic acid residues each having a free carboxyl group. Both inner core and lipid A part contain phosphates. On the phosphates, ester-linked substituents carrying a free amino group reduce the net negative charge of LPS [71].

26

Salmonella enterica is a type of Gram-negative bacteria. *Salmonella* species are intracellular pathogens [72]. Some serotypes can cause illness, for example *Typhimurium* [73]. To be able to prosper in hosts that can produce antibacterial peptides, it is necessary for *Salmonella* to show resistance to these peptides. This is essential for *Salmonella* virulence [74]. And it has been found that the *phoP* gene is a regulator for *Salmonella typhimurium* virulence. The *Salmonella typhimurium* PhoP/PhoQ activated gene *pagP* is required for the biosynthesis of hepta-acylated lipid A. The mutant *Salmonella* strains whose *phoP* gene is repressed are avirulent [75, 76].The extracellular Mg^{2+} concentration modulates the whole PhoP/PhoQ system and with this the virulence of *Salmonella typhimurium*. In low extracellular Mg^{2+} concentration, PhoQ phosphorylates PhoP, resulting in the expression of PhoP-activated genes and repression of PhoP-repressed genes. In contrast, under high extracellular Mg^{2+} concentration, PhoQ dephosphorylates PhoP, leading to the repression of PhoP-activated genes and may contribute to the expression of some PhoP-repressed genes [77, 78].

To get a better understanding of these complex behaviors of *Salmonella typhimurium*, a bulk analysis is insufficient. It is crucial to understand how a single bacterium reacts to the external environment. In the past 30 years, AFM has revolutionized how researchers probe the microbial cell surface. It can reach a resolution of a few nm [79]. After cells are well attached to a suitable solid substrate, the images of single cells like *Lactobacillus rhamnosus* GG, *Lactococcus lactis*, and *Lactobacillus plantarum* were obtained [80-83]. The major differences in cell surface architecture for these three Gram-positive bacteria

species were revealed. *L. rhamnosus* GG had a rough surface morphology decorated with 15 nanometer-high wave-like structures [81]. However, 25 nanometer-wide striations documenting peptidoglycan cables that run parallel to the short cell axis were found in *L. lactis* [80]. Similar nanocables were observed on purified sacculi from *Bacillus subtilis* [83]. By contrast, *L. plantarum* showed a highly polarized surface morphology with smooth poles and rough side walls [82]. Using AFM, Umeda et al. were also able to distinguish between Gram-negative bacteria and Gram-positive bacteria based on the wavy surface appearance of the former [84]. Besides imaging the surface morphology of single cells, AFM was used to examine the effects of surface potential on methicillin-resistant *Staphylococcus aureus* USA 100's adhesion to medically relevant surfaces such as steel and gold [85].

In order to get additional insights into how the *phoP* affects the outer membrane structures and its surface potential distributions, we adopted AFM to analyze the surface roughness and surface potential distributions of wild and mutant strains grown under different concentrations of Mg^{2+}.

3.2 Materials and Methods

3.2.1 *Salmonella Typhimurium* Culture

Salmonella typhimurium strains culture conditions can be found in [86]. After collecting the cultured bacteria, four test tubes were prepared: Two of them have high Mg^{2+} concentration ($10\ mM$), the other two with low Mg^{2+} concentration ($10\ \mu M$). The four different bacteria samples would be wild type *Salmonella typhimurium* grown under high

Mg^{2+} concentration (w.t. high Mg^{2+}), wild type *Salmonella typhimurium* grown under low Mg^{2+} concentration (w.t. low Mg^{2+}), *phoP* mutant *Salmonella typhimurium* grown under high Mg^{2+} concentration (*phoP* high Mg^{2+}) and *phoP* mutant *Salmonella typhimurium* grown under low Mg^{2+} concentration (*phoP* low Mg^{2+}).

3.2.2 Gold-Coated Glass Surface Preparation

For KPFM measurements, conductive substrates are required. We used gold-coated glass substrates (Arrandee[TM], Au (111) on glass, 11x11 mm) for this purpose. The substrates were sonicated in acetone, ethanol and deionized water for 5 mins each, and dried under a stream of pure nitrogen gas. The substrates were coated with 40 μL of 0.1% poly-L-lysine for 40 minutes and rinsed with deionized water. The bacteria sample solutions were deposited on the substrate for 1 h. Finally, the substrates were rinsed thoroughly with 1x PBS and dried with nitrogen gas for AFM imaging.

3.2.3 Root Mean Square Roughness and Surface Potential Analysis

Root mean square (RMS) roughness is one of the most used amplitude parameters. It is used to study temporal changes in the creation of a new surface as well as spatial differences when studying the surface feature using different scales. According to [87, 88], the RMS roughness R_{rms} is given by the standard deviation of the data:

$$R_{rms} = \sqrt{\frac{\sum_{n=1}^{N}(z_n - \bar{z})^2}{N-1}}$$

where $\bar{z}$ is the average of the z values within the analyzed area, z_n is the current z value and N is the data points within the given area. Other definitions can also be used to characterize the roughness, such as the mean roughness (the mean value of the surface relative to the center plane) or the peak-to-valley distance (the distance between the highest data point and the lowest data point of the surface). However, these definitions are usually less accurate than the RMS roughness. In the peak-to-valley distance, only two points of the scanned surface (namely the highest and the lowest) are taken into account, which is not very representative of the whole surface. A comparison between the RMS and the mean roughness shows that the latter takes less account of the variations of the low frequencies. Hence the RMS roughness is the most accurate and will be used in the rest of this chapter [87, 88]. The size of our topography images is 3.5 μm times 3.5 μm containing 512 times 512 pixels. 10 single *Salmonella typhimurium* cells were analyzed for each different bacteria sample. To minimize the effect of the curved cell surface and to cover as much of the cell surface as possible, the roughness of three separate areas with 100 times 100 pixels on the cell surface were analyzed. An average roughness from the three roughness values was obtained for a single cell. Then a final average roughness for each of the four *Salmonella typhimurium* bacteria samples was calculated using the 10 average roughness values.

To obtain the surface potential distributions for the four bacteria samples, the surface potential distributions of 10 *Salmonella typhimurium* cells for each type were obtained. This time, the surface potential distribution of a single cell was obtained by analyzing the surface potential of each pixel on the cell surface. All parts of the cells' surface were

covered. The surface potential distributions of 10 cells went through box plot statistical analysis to obtain the final surface potential distribution for each different bacteria sample. And Wilcoxon-Mann-Whitney test was used to check the statistics results.

3.3 Results and Discussions

We used two-pass KPFM to study *Salmonella typhimurium* cells. During the first pass of two-pass KPFM, the AFM is operating under normal tapping mode. The topography of the bacteria was obtained as seen in Fig 3-1. Then, the cantilever was lifted to 30nm above the surface for measuring the surface potential distribution. The surface potential distributions for wild-type *Salmonella typhimurium* and *phoP* mutant under high and low Mg^{2+} conditions were obtained this way. They are shown in Fig 3-1.

i

0.14 µm

-0.07 µm

x: 3.5 µm

y: 3.5 µm
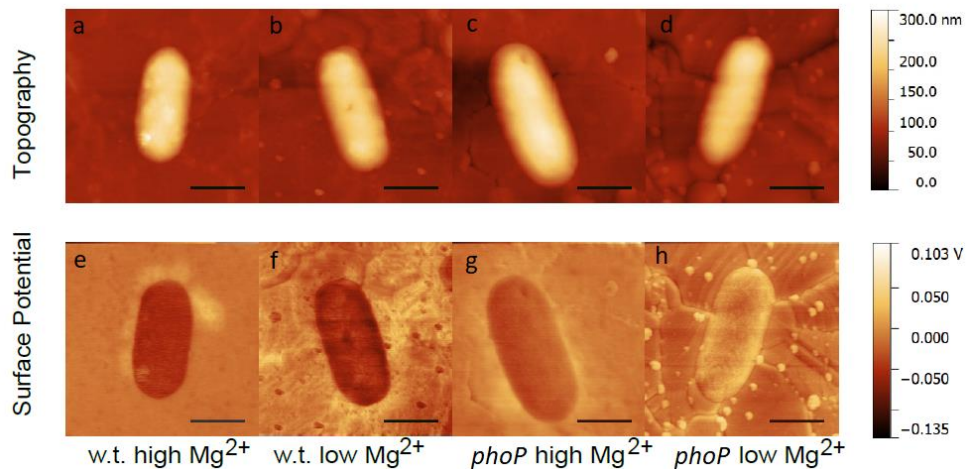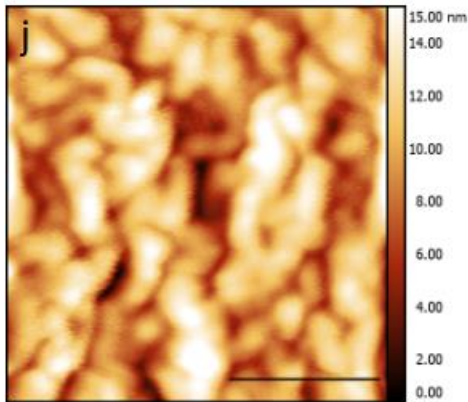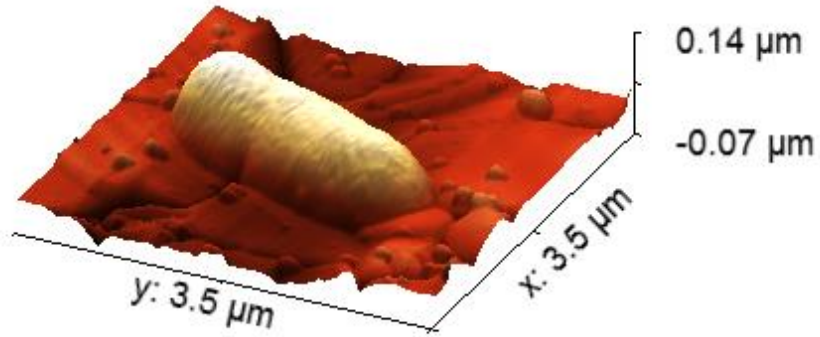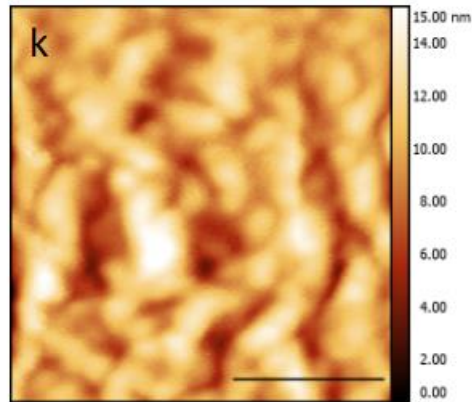
w.t. high Mg^{2+}

w.t. low Mg^{2+}
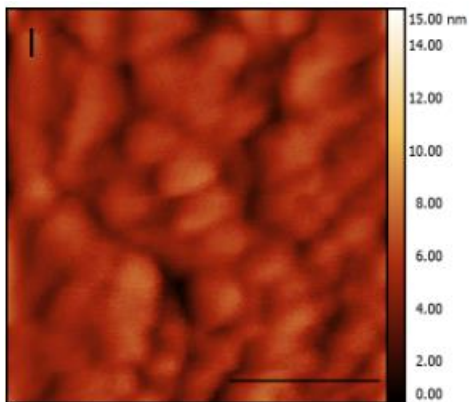
phoP high Mg^{2+}
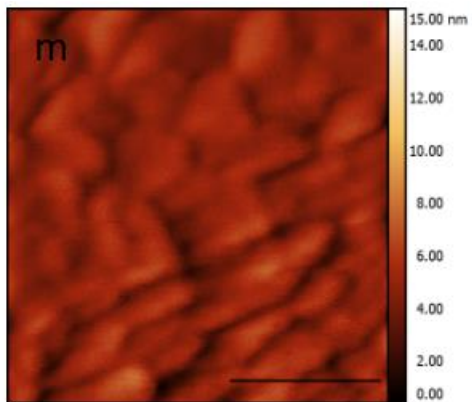
phoP low Mg^{2+}

Fig 3-1. *Salmonella typhimurium* **bacteria topography and surface potential images.** (a) to (d) Topography images of wild type and *phoP* mutant type *Salmonella typhimurium* under high and low Mg^{2+} conditions. (e) to (h) Surface potential distributions of these bacteria under high and low Mg^{2+} conditions. The scale bar is 1 μm for images (a) to (h). (i) 3D representation of image (d). Zoomed-in images of the four bacteria surfaces are included from (j) to (m). The scale bar for images (j) to (m) is 200 nm.

The RMS roughness analysis results are shown in Fig 3-2. Wild-type *Samonella typhimurium* showed a higher roughness comparing to the mutant ones. Wild-type *Salmonella typhimurium* bacteria grown under high Mg^{2+} and low Mg^{2+} have an average roughness of 6.6 ± 0.9 nm and 6.0 ± 1.3 nm respectively while *phoP* high Mg^{2+} has an average roughness of 5.3 ± 1.1 nm and *phoP* low Mg^{2+} has an average roughness of 5.6 ± 1.5 nm. W.t. *Salmonella typhimurium* grown under high Mg^{2+} concentration has the highest average roughness among all the four types of samples. And *phop* mutant *Salmonella typhimurium* grown under low Mg^{2+} concentration showed the lowest average roughness.
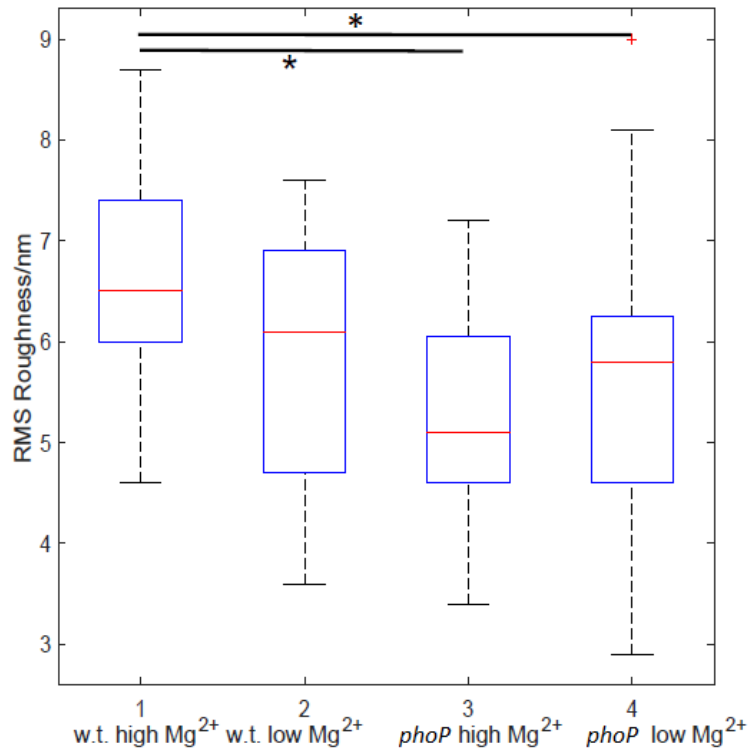
Fig 3-2. Bacteria outer membrane roughness comparisons. We found that w.t. bacteria have higher roughness than *phoP* mutant bacteria. Significance tests show that w.t. bacteria grown under high Mg^{2+} concentrations have significantly different RMS roughness value from *pho*P mutant bacteria grown under high and low Mg^{2+} concentrations. Wild-type bacteria grown under high and low Mg^{2+} concentrations show no significant differences in RMS roughness.

Utilizing KPFM, we measured the surface potential of *Salmonella typhimurium* bacteria under ambient conditions. The average surface potentials of the four bacteria samples were

obtained. W.t. *Salmonella typhimurium* grown under high and low Mg^{2+} concentrations have negative average surface potentials of -65 ± 23 mV and -71 ± 27 mV respectively. *phoP* high Mg^{2+} has a negative average surface potential of -40 ± 19 mV as well. In contrast, *phoP* low Mg^{2+} showed a positive average surface potential of 20 ± 33 mV. The results are shown in Fig 3-3. W.t. low Mg^{2+} showed a relatively lower surface potential comparing to w.t. high Mg^{2+}.
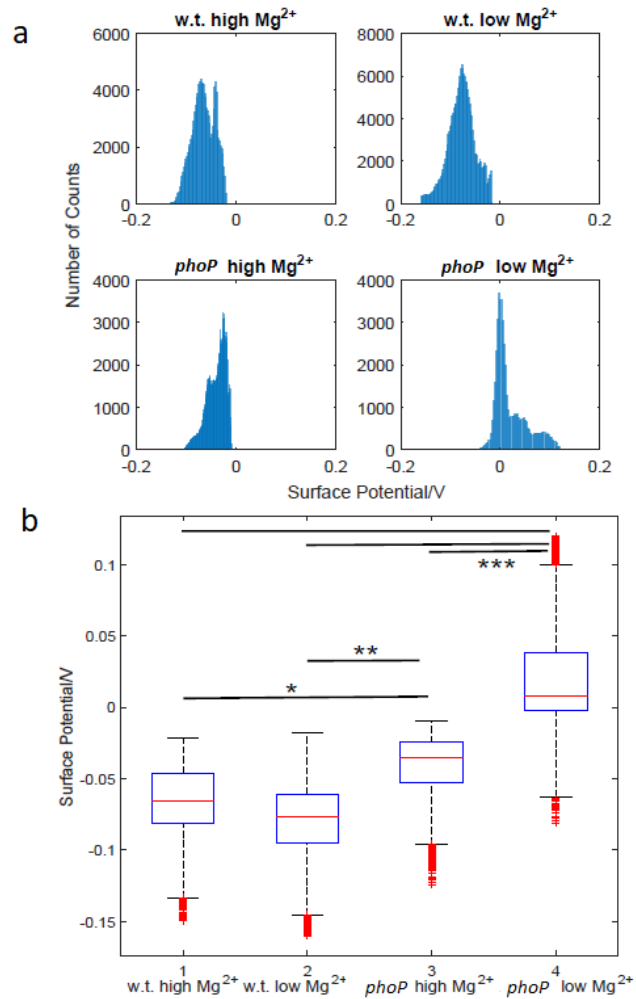
** represents p<0.005   *** represents p<0.0005

Fig 3-3 Bacteria surface potential comparisons. (a) shows the histograms of surface potential distributions for the two strains under the different Mg^{2+} conditions. (b) represents the statistical analyses for the surface potential distributions. Comparing to other bacteria, *phoP* mutant bacteria grown under low Mg^{2+} concentrations have significantly different surface potentials.

Ionic interactions within the core and lipid A region are known to be critical in forming the permeability barrier of LPS [89], which are important for the virulence of *Salmonella typhimurium*. And according to [77], Mg^{2+} modulates complex phenotypic properties which are related to the virulence of *Salmonella* through regulating *phoP* gene expression. *phoP* regulates the transcription of genes that result in modifications of lipid A, such as addition of aminoarabinose to lipid A phosphate groups, replacement of the lipid A acyl group myristate with 2-OH myristate and the formation of heptaacylated lipid A by the addition of palmitate [90, 91]. For *phoP* mutant *Salmonella typhimurium* bacteria, these modifications of lipid A will not happen. This will lead to significant surface characteristics variations from wild type *Salmonella typhimurium* bacteria as lipid A is a major component of LPS and LPS is the major surface molecule of *Salmonella typhimurium* outer membrane. The missing of these lipid A modifications might lead to the smaller roughness and higher surface potential of *phoP* mutant *Salmonella typhimurium*.

3.4 Conclusions

Through AFM tapping mode, we found that w.t. *Salmonella typhimurium* bacteria surface roughness is *phoP* dependent. *phoP* gene is regulating the virulence of *Salmonella*

36

typhimurium. And the roughness of *Salmonella typhimurium* grown under different Mg^{2+} concentrations show roughness variations as well. This is related to the role of Mg^{2+} in modulating complex phenotypic properties of *Salmonella typhimurium* surface. Using KPFM, we found that w.t. *Salmonella typhimurium* bacteria have negative surface potential. *phoP* low Mg^{2+} showed positive surface potential while *phoP* high Mg^{2+} surface potential stayed negative. This might be because low Mg^{2+} can trigger the activation of several genes that are related to the virulence of *Salmonella typhimurium* except for *phoP* [86, 91]. These results will help shed light on the roles of the *phoP* gene and Mg^{2+} on the virulence of *Salmonella typhimurium*. And they will help us get a better idea about how to control the virulence of some infectious Gram-negative bacteria by manipulating their surface roughness and surface potential. A direct map between different LPS structure modifications and surface roughness and surface potential variations could also be constructed in further study. It might help identify the virulence of one type of bacteria through AFM roughness and surface potential measurements which can be done in a short time.

CHAPTER 4

RECOGNITION IMAGING ON NATIVE CHROMATIN EXTRACTED FROM

CANCEROUS AND NON-CANCEROUS CELL LINES

4.1 Introduction

Eukaryotic genomes are packaged with octameric protein complexes, consisting of two copies each of histones H2A, H2B, H3 and H4, which wrap nearly two turns of DNA to form nucleosomes [51]. Since the discovery of nucleosomes in the early 1970s, a variety of techniques have been applied to their study. However, both ultrastructural technologies (e.g., crystallography and electron microscopy) and biochemical analyses (e.g., nuclease assays and sedimentation) have been limited in their scope, because they cannot simultaneously assay structure and dynamics. Over the years, progress has been made in applying technologies that have the potential to bridge the gap between static ultrastructural features and dynamic physiological processes in the study of chromatin. These technologies, which include scanning confocal fluorescence microscopy [92], optical tweezers [93, 94] and atomic force microscopy (AFM) [30, 95], have provided remarkable insights into the behavior of individual nucleosomes. The combination of single-molecule resolution, and observation of native macromolecular complexes has made AFM especially attractive for studying nucleosomes [95].

In our experiments, we applied AFM recognition imaging directly to native human chromatin samples to study the native human chromatin forming components. For recognition imaging, the ultra-sensitive MAC mode, driving the cantilever oscillation, is

commonly use [37]. Commercial MAC mode probes are typically made of silicon nitride or quartz. We developed a protocol to coat sharp commercial silicon probes with nickel making them reliable MAC mode probes.

We applied our new probes to samples prepared from the supernatant fraction of a salt fractionation for EPC2 (non-cancerous) and CPD (cancerous) esophageal cell lines. Salt fractionation is an efficient method for the extraction of intact chromatin fragments from cell nuclei [96]. With anti-H3 antibodies modified MAC mode probe, we identified histones H3 in samples of both cell lines, indicating that this fraction contains chromatin.

To get more information about the binding specificity of anti-H3 antibodies to histones H3 in our samples, we added H3 peptide (abcam, Product#, ab12149) to the flow cell during our recognition imaging with both EPC2 and CPD cell lines. This method was used in imaging glycosylation [97] and lysozyme [37]. We proved the specificity by blocking with a peptide mimicking the H3 binding site for our antibody. Further, we demonstrated the dependence of the recognition signals on the oscillation amplitude of the probe, indicating the robustness of our recognition signals.

With the reliability of AFM recognition imaging in mind, we further analyzed the components of extracted chromatin from the supernatant fraction for both EPC2 and CPD cell lines. SMC2, a structural maintenance protein for chromosomes, is a component of the condensin complex, an important player in chromatin organization in the nucleus. We applied AFM recognition imaging with anti-SMC2 antibody modified probes to the

prepared chromatin samples and identified SMC2 proteins in samples of both cell lines. Western blot data confirms the presence of SMC2 proteins in the samples.

Overall, AFM recognition imaging provides a robust way to analyze the structure and molecular components of extractions from human cells. This will help to get insights into the link between chromatin structure and cell phenotypes.

4.2 Materials and Methods

4.2.1 MAC Cantilevers Fabrication

Homemade MAC cantilevers were used for recognition imaging. To prepare MAC cantilevers, SHOCON Si cantilevers (spring constant k = 0.14 N/m, resonance frequency f = 21 kHz) from APPNANO were used. We found that coating the Si cantilevers with 1 nm titanium (Ti) and 20 nm nickel (Ni) resulted in the best results for MAC mode imaging. The coatings were conducted with Lesker #1 Sputter equipment in the NANOFAB core in ASU. During the coating process, the sputtering speed of titanium was selected to 0.1 Å/s and nickel was selected to 1 Å/s.

4.2.2 Imaging of MAC Cantilever Tip with Transmission Electron Microscopy

A technique called focused ion beam (FIB) was combined with transmission electron microscopy (TEM) to image the thickness of coatings of our homemade MAC cantilevers. A TEM lamella was lifted out from the AFM tip using Helios 5 UX dual-beam microscope (ThermoScientific). A 500nm carbon (C) protection layer of 14µm by 4µm size followed

by a 500nm of tungsten (W) protection layer of 13µm by 3µm size were deposited by e-beam induced deposition on the back side of the AFM tip. An additional 2µm of Tungsten protection layer of 12µm by 2µm size was deposited via ion beam induced deposition. The focused ion beam in the same tool was used to mill a lamella around the protection layers, which was then lifted out using the Easy Lift equipped with the microscope. The lamella was then thinned using low ion beam currents (243pA then 40pA at 30kV) followed by a 2kV cleaning with 68pA ion beam current. The final thickness of the lamella is ~60nm. The TEM imaging of the lamella was done using JEOL 2010F at 200kV. The thickness of the Ni layer was then measured using Gatan DigitalMicrograph software.

4.2.3 MAC Cantilevers Functionalization

The MAC cantilevers functionalization method was adapted from [98]. To functionalize the MAC cantilevers, we first cleaned the cantilevers in chloroform (CH_3Cl) for three rounds. After that, the cantilevers were cleaned in oxygen plasma (Harrick Plasma) under high condition for 30 s. The cantilevers were then placed inside of a desiccator. 30 μL APTES and 10 μL triethylamine were added to the desiccator. The desiccator was vacuumed for 30 mins. Then the desiccator was kept under vacuum for one hour. 1 mg of MAL-dPE®$_{24}$-NHS ester (bought from Quanta Biodesign, Product#, 10314) was dissolved in 1 mL CH_3Cl with 5 μL triethylamine. After the cantilevers were modified by APTES, they were placed in the above solution for 2 to 3 h. Then, the cantilevers were rinsed in chloroform and dried in air.

Next, the functionalized cantilevers were placed in SATP (N-succinimidyl 3-

(acetylthio)propionate) modified antibody solution. One functionalized cantilever is illustrated in Fig 4-2 (a) in section 4.3.

Two types of antibodies were used, anti-H3 (Abcam, Product#, ab1791) and anti-SMC2 (Abcam, Product#, ab10399). The concentration of the stock solution of both antibodies was 1 mg/mL. First, 10 μL of the desired antibody stock solution was diluted to 100 μL in buffer A (100 mM N$_a$Cl, 50 mM NaH2PO4, 1 mM EDTA, pH 7.5). The 100 μL diluted antibody solution was placed in the deionized pre-wetted dialysis tube (D-tube™ dialyze mini MWCO 6-8 kDa, EMD Millipore, product#, 71504-3) and floated in a beaker with 500 mL of buffer A for three hours with gentle stirring. After 3 h, the tube was removed. The desalted antibody solution was mixed with 125 μL (usually, the volume of desalted antibody solution would increase to around 125 μL) DMSO with a 10-fold molar excess of SATP and stirred under nitrogen for 30 mins. The total volume of the reaction mixture would be larger than the maximum volume one dialysis tube can hold. It was split into two pre-wetted dialysis tubes, which were floated in buffer A for another 3 h. After the antibody was modified by SATP, the PEG linker-bound cantilevers were incubated in 50 μL SATP-antibody, 25 μL NH$_2$OH-reagent (500 mM NH$_2$OH·HCl, 25 mM EDTA, pH 7.5) and 50 μL buffer A for 1 h. Then the functionalized cantilevers were rinsed once with buffer A and once with 1x PBS buffer (150 mM NaCl, 5 mM Na$_2$HPO$_4$, Ph 7.5). The rinsed cantilevers were placed inside of 1x PBS buffer and stored in a 4 ℃ fridge for later use. We found that the probes are stable for at least 1 month.

4.2.4 Chromatin Samples Preparation

Two types of cell lines were used in the experiment, a normal human esophageal cell line (EPC2) and a cancerous human esophageal cell line (CPD) with high-grade dysplasia. After about 50 million cells were grown, the cells were collected to an Eppendorf 15 mL tube. Then these cells were spun down at 1000 RPM for 5 min at 4 ℃. After that, the supernatant part was removed and the cells were resuspended in 10 ml of cold PBS and spun down again at 1000 RPM for 5 min at 4 ℃. The supernatant part was removed again and the cells were resuspended in 10 ml of cold PBS with 0.1% tween (10 µl for every 10 ml of PBS) and spun down at 1000 RPM for 5 min at 4 ℃. Next, the supernatant part was removed once more and 10 ml of 0.5% NP-40 in TM2 buffer (20 mM Tris, 2 mM $MgCl_2$) with 0.5 mM phenylmethylsulfonyl fluoride (PMSF) was added into the tube to resuspend the cells. The tube was vortexed lightly and then set on ice for two minutes. Then the cell lysates were spun down at 1000 RPM for 10 min at 4 ℃ without break for one more time. A white "fluffy" looking pellet can be seen in the tube. After the supernatant part was removed, the pellet was resuspended in 10 ml of TM2 buffer with 0.5mM PMSF (50 µl of 100 mM PMSF). For the last time, the cell lysates were spun down at 1000 RPM for 5 min at 4 ℃. The supernatant was removed again. The extracted cell contents were resuspended in 2 ml of 0.1 TE (10 mM Tris, 1 mM EDTA) with 0.5 mM PMSF (10ul of 100 mM PMSF). The nuclei resuspension was split into two Eppendorf tubes for later use. Chromatin extractions in the cell lysates of two cell lines were digested by micrococcal nuclease (MNase, TheromoFisher Scientific, Product#, 88216) for 4 mins (or 8 mins). Then the digested samples were centrifuged under 1600 rpm for 10 mins with just supernatant collected later. The collected supernatant samples were cross-linked by 0.5%

glutaraldehyde for 15 mins and diluted 100 (or 1000) times by TE buffer (TEKNOVA, catalog#, T0228).

Substrates used in the experiment are mica (Ted Pella, Product#, 56-75). Mica was first cut into square chips with a side length of about 2.2 cm. 4 mica chips were cleaved by Scotch tape and placed in a plastic petri dish. 80 μL APTES was added to one glass vial and 15 μL triethylamine was added to another one. Together with the two glass vials, the petri dish is placed inside a desiccator. Similar to functionalizing cantilevers with APTES (see above), the mica chips were coated with APTES. 4 μL of the above diluted samples were dropped onto APTES modified mica surfaces. The substrates were incubated in a humid chamber for 30 mins and rinsed thoroughly with 1x PBS before imaging.

4.3 Results and Discussions

We imaged the coatings of our homemade MAC cantilevers using TEM (Fig. 4-1). The total thickness we got from TEM has an average value of 27.9 ± 0.2 nm (Fig 4-1 (b)). These homemade MAC cantilevers were tested and the sensitivity result is shown in Fig 4-1 (c).
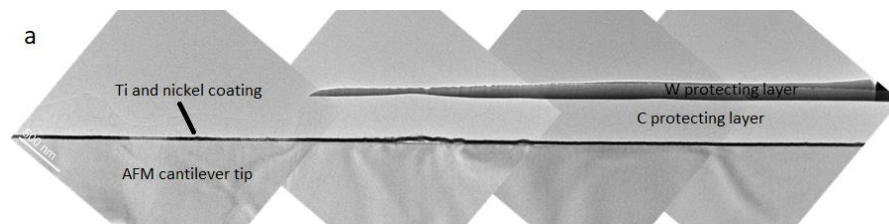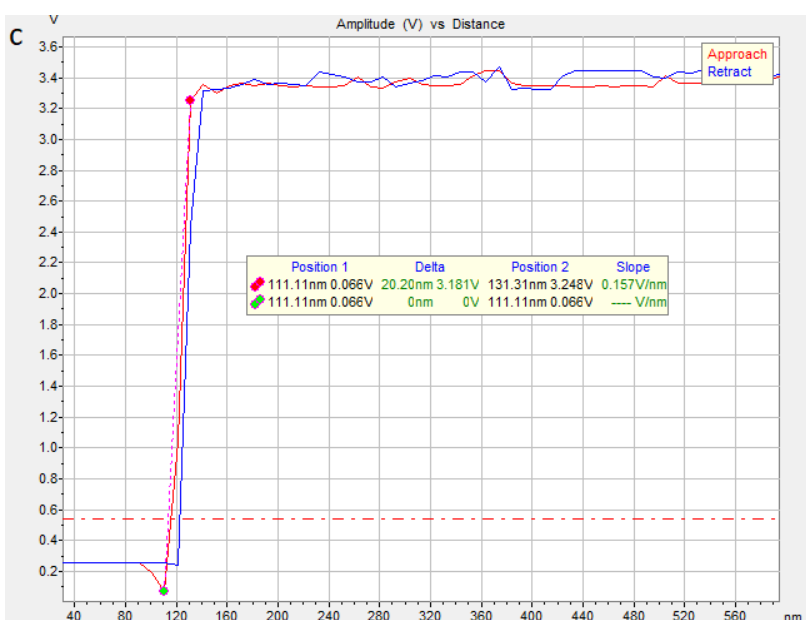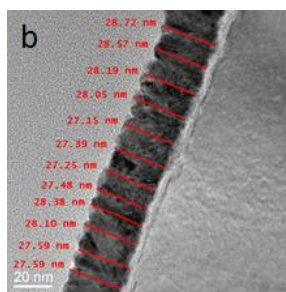
Fig 4-1 TEM image of a cantilever tip lamella after FIB preparation with coating thickness measurements and the sensitivity of a MAC cantilever. (a) is the TEM image of a cantilever tip lamella. (b) indicates the thickness of the coating. (c) shows the sensitivity of one MAC cantilever.

Histones are a major component of nucleosomes. One major family member of histones is H3. We used anti-H3 antibodies for our recognition imaging experiments. The images were taken in 1x PBS solution. As shown in Fig 4-2 (b) and (e), both EPC2 and CPD show recognition signals for anti-H3 antibodies, which indicates the existence of histones H3 in our prepared samples. To get an idea of how the topography signals and recognition signals

correlate, a superimposition of topography and recognition images was conducted for both cell lines. In Fig 4-2 (c) and (f), in order to see the overlay clearly, green and red colors were used for the topography and recognition images respectively. Red dots in the overlay image represents recognition signals.

However, the orientation of H3 histones on the substrates will vary from nucleosomes to nucleosomes. And unlike reconstructed chromatin samples from previous research [99], Further, H3 histones are not the only histone components in our chromatin samples. And many other proteins that interacts with DNA will be in our samples because of cross-linking. It would be not possible to expect similar recognition levels for all the single nucleosomes in our samples.
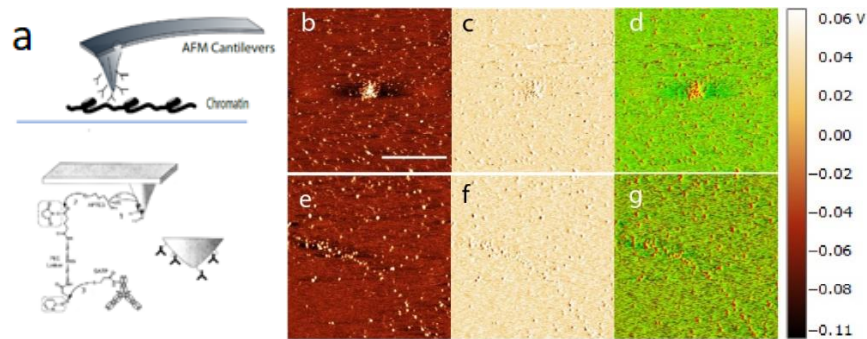
Fig 4-2. AFM recognition imaging of chromatin illustration and recognition images of EPC2 and CPD supernatant chromatin. MAC cantilevers were functionalized with APTES and then modified with anti-H3 antibodies (a). The molecules illustrations are adapted from [98]. Anti-H3 antibodies are IgG antibodies which are shown as the 'Y' shapes attaching to the cantilever through PEG-linkers. EPC2 and CPD supernatant

chromatin was extracted and cross-linked and then attached to APTES modified mica substrates (a). Images (b) and (c) are topography and recognition images for EPC2 chromatin sample. Images (e) and (f) are for CPD. Dark points in (c) and (f) indicate authentic recognition signals. And images (d) and (g) are the overlay of topography and recognition images. They match each other well. The scale bar shown in (b) represents 400 nm. The scan sizes of all AFM images is 1 μm x 1 μm.

To get a better understanding of the binding between anti-H3 antibodies and histones H3 in our supernatant samples under AFM recognition imaging, we analyzed the recognition signal magnitudes in our images. According to [100], appropriate oscillation amplitudes of cantilevers are critical for antibodies binding to antigens to get recognition signals. The PEG linker used in the experiments consisted of 24 units, which correspond to an unstretched contour length of 10 nm long. For the linker to stretch completely, the oscillation amplitude of the cantilever should be in the range of the linker length. If the oscillation amplitudes of cantilevers are too high, recognition signals will be lost. Like the insets in Fig 4-3 (b) for EPC2 cell line and (f) for CPD cell line, two typical recognition curves under appropriate cantilever oscillation amplitudes between 10nm and 20nm show signal levels higher than 0.05 V. However, when the oscillation amplitude of the cantilever increased to 30nm, signal blocking will appear. As shown in (d) and (h), the signals are less than 0.05 V considering and can be considered as background. After analyzing images from both EPC2 and CPD cell lines, the distributions of recognition signals and blocked signals are shown in Fig 4-4. A threshold level of about 0.05 V for recognition can be

identified from the distributions. Signals that are higher than 0.05 V are considered recognition signals while other signals are excluded from this category.
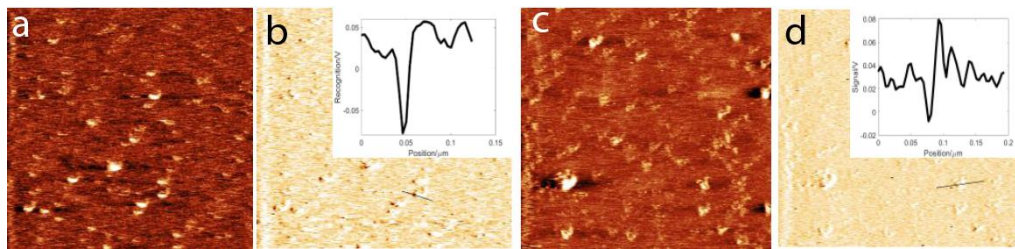
EPC with an amplitude of 10 nm   EPC2 with an amplitude of 30 nm
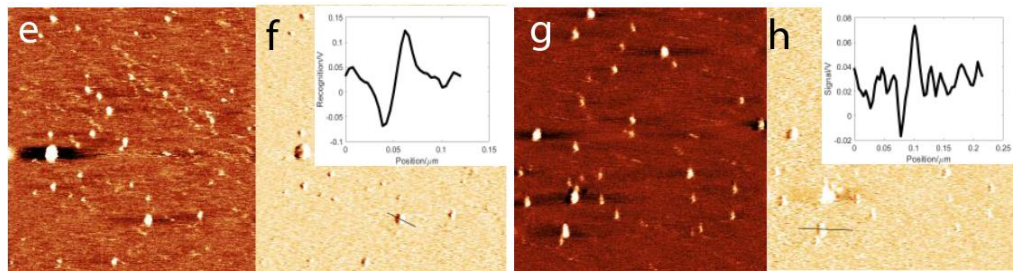
CPD with an amplitude of 18 nm   CPD with an amplitude of 31 nm

Fig 4-3. Anti-H3 recognition imaging results under small and large cantilever oscillation amplitudes. As seen from (b) and (f), as the oscillation amplitude of the cantilever was within some appropriate range (10 and 18 nm), PEG-linker could stretch properly and recognition events can be detected. When the oscillation amplitude of the cantilever was over the appropriate range, recognition events would be blocked. That can be seen in (d) and (h), where the oscillation amplitudes of the cantilever were about 30 and 31 nm separately. The insets in (b), (d), (f), and (h) show signal curves along chosen nucleosomes.
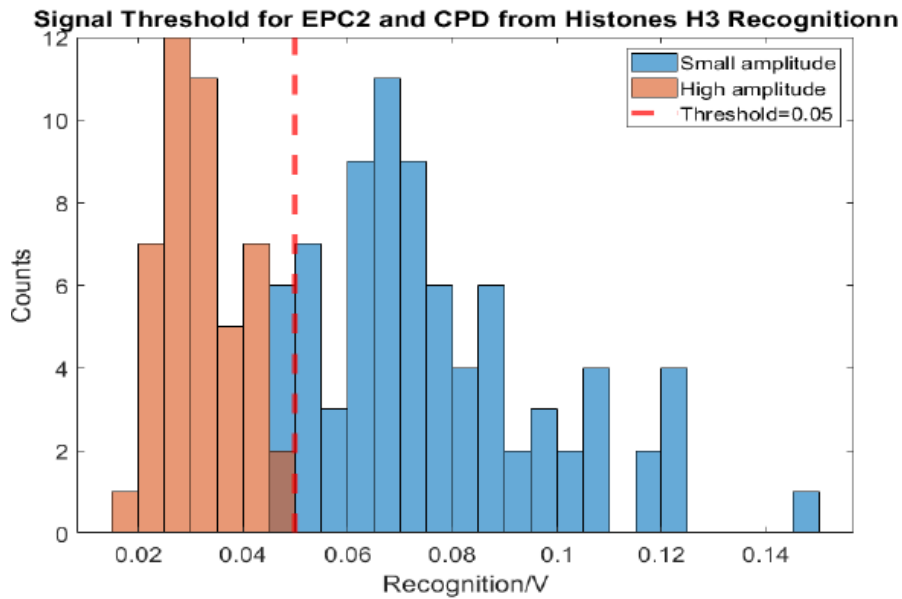
Fig 4-4. Recognition signals and blocked signals distributions. The distributions are constructed using signals from both EPC2 and CPD anti-H3 recognition images under small and high cantilever oscillation amplitudes. Under small oscillation amplitudes of the cantilever, due to the complete stretch of PEG-linkers, we saw normal recognition signals. Under high oscillation amplitudes of the cantilever, signal levels decreased by a large amount. Combining the signal distributions for the two situations, a recognition threshold of 0.05 V was determined.

Even though the binding between antigen-antibody is specific, there might be non-specific binding happening during imaging. According to the threshold we have found, signals above 0.05 V are authentic recognition signals. Otherwise, the signals will be assumed to come from non-specific bindings.

To check the specificity of our recognition signal between anti-H3 and histones H3, we applied H3 peptide in our experiments. The final concentration of H3 peptide in the flow cell was about 60 $\mu g/mL$. After adding H3 peptide into the flow cell, those peptides bound to the exposed anti-H3 antibodies on the cantilevers, reducing the binding between anti-H3 antibody and histones H3 in the prepared samples. That is consistent with our results. Fig 4-5 (a) and Fig 4-5 (b) are the topography and recognition images of EPC2 cell line before adding H3 peptide. Fig 4-5 (d) and Fig 4-5 (e) are the topography and recognition images of EPC2 cell line after adding H3 peptide for about 1 hour. The imaging spots for these images are the same as indicated by the arrows in the topography images. Adopting the recognition signals threshold identified above, we analyzed in detail the signal levels for nucleosomes in Fig 4-5. Nucleosomes with signal levels higher than 0.05 V in Fig 4-5 (b) and Fig 4-5 (e) were counted. After comparing to the total number of nucleosomes in Fig 4-5 (a) and Fig 4-5 (d), we found out that 53.7% of nucleosomes have signal levels higher than 0.05 V for Fig 4-5 (b) while only about 38.3% nucleosomes showed signal levels above 0.05 V for Fig 4-5 (e). The results for CPD chromatin are shown in Fig 4-6. From both the results for EPC2 and CPD chromatin, we can conclude that our observed recognition signals are specific and H3 is present in our samples.
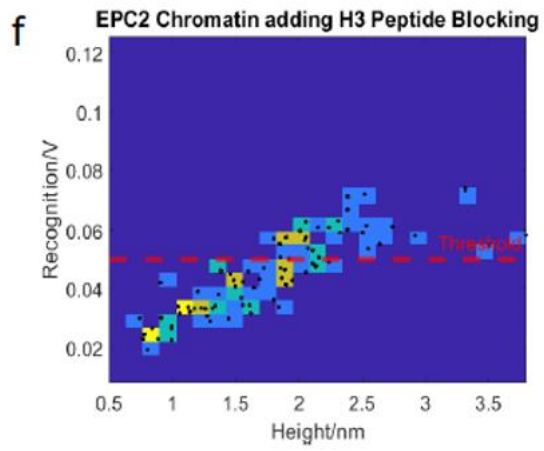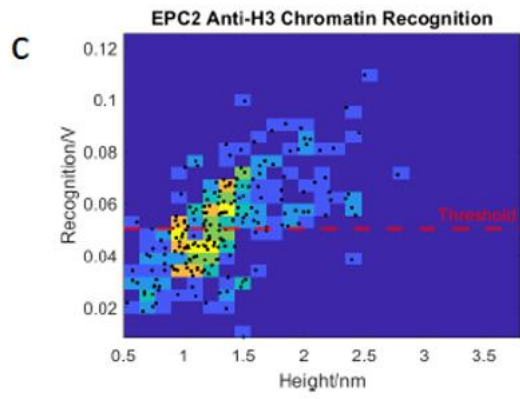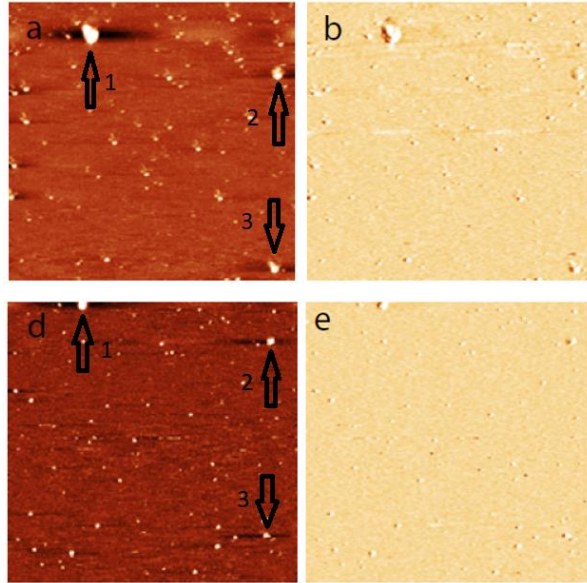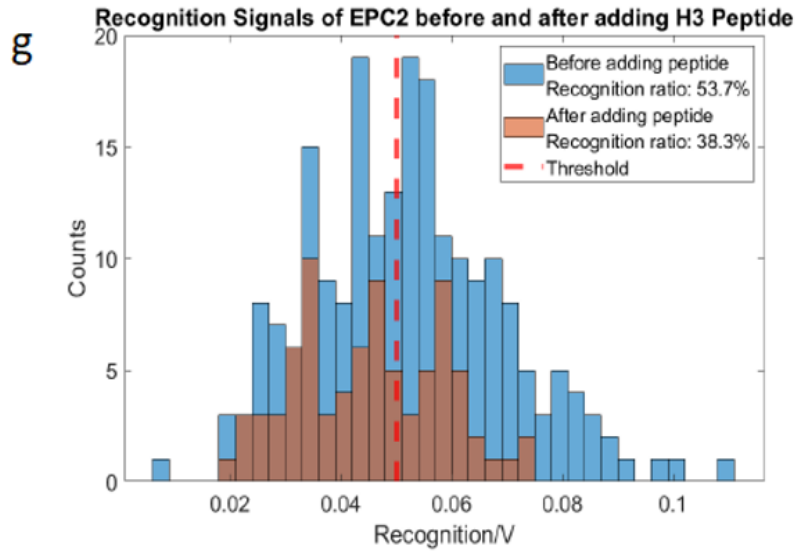
Fig 4-5. EPC2 chromatin anti-H3 recognition before and after H3 peptide blocking and the related correlations between topography and recognition. We analyzed the correlations between recognition signals and nucleosome sizes before and after adding peptides, which can be seen in (c) and (f). Peptide blocking will shift the threshold of nucleosome sizes from where recognition signals can be seen. And according to (g), the recognition ratio before adding H3 peptide was higher than after peptide blocking.

a b

d e

c

CPD Chromatin Anti-H3 Recognition

Threshold

Recognition/V

0.12
0.1
0.08
0.06
0.04
0.02

0.5 1 1.5 2 2.5 3 3.5
Height/nm

f

CPD Chromatin adding H3 Peptide Blocking

Threshold

Recognition/V

0.12
0.1
0.08
0.06
0.04
0.02

0.5 1 1.5 2 2.5 3 3.5
Height/nm

g

Recognition Signals of CPD before and after adding H3 Peptide
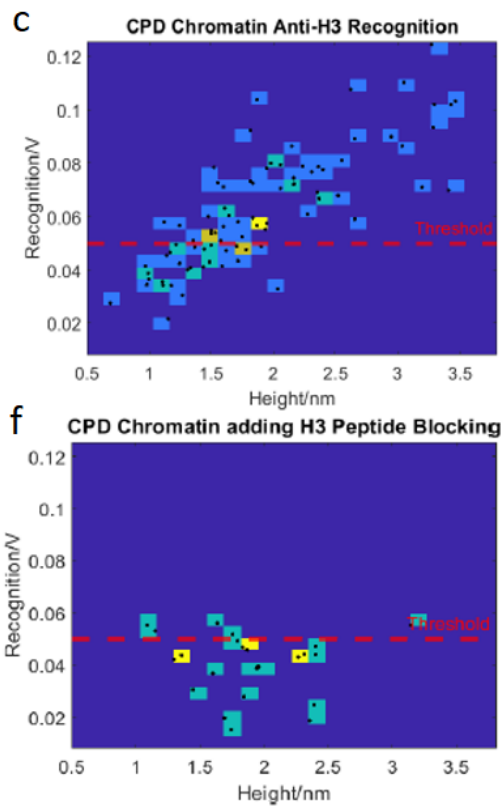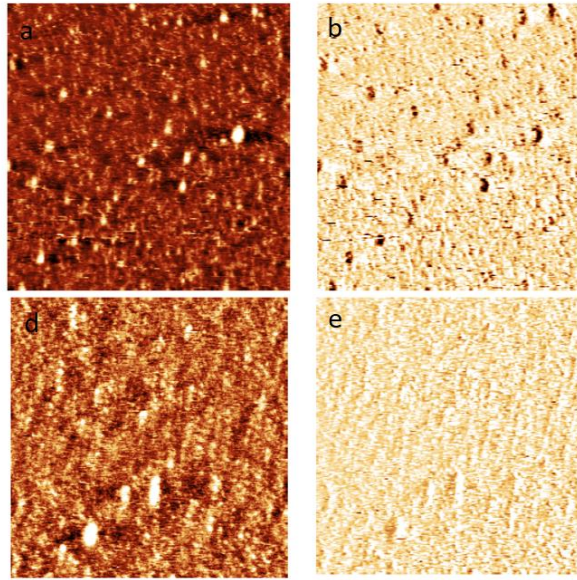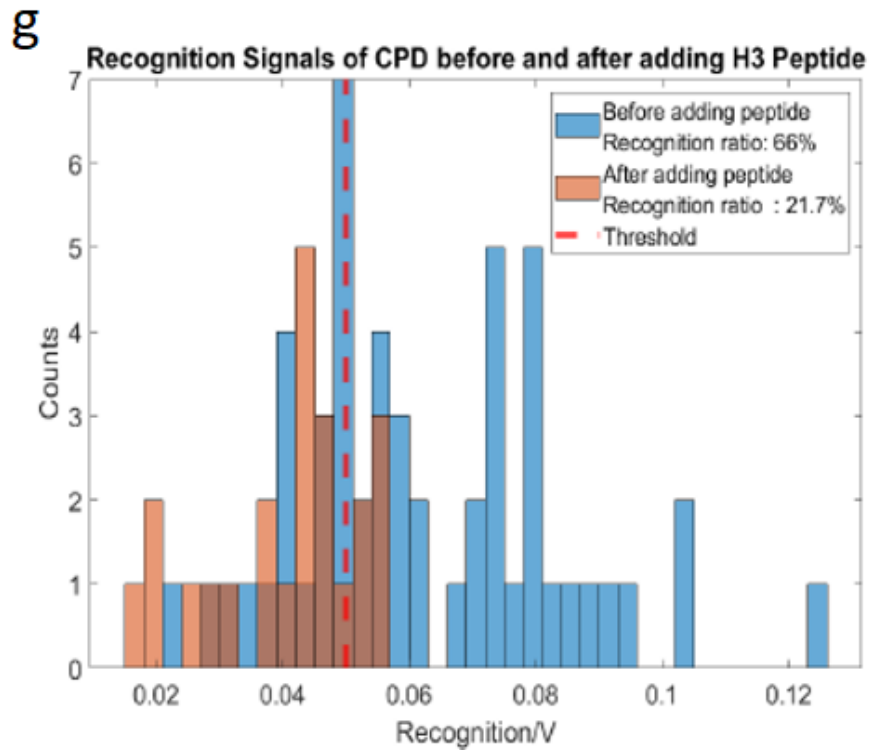
Fig 4-6. CPD chromatin anti-H3 recognition before and after H3 peptide blocking and the related correlations between topography and recognition. (a) and (b) are CPD chromatin topography and recognition images before adding peptide. (d) and (e) are CPD chromatin topography and recognition images after adding peptide 1 h. (c) and (f) shows the correlations between recognition signals and nucleosome sizes before and after adding peptides. And (g) illustrates the recognition ratio before and after adding peptide.

We extended our study of native chromatin form EPC2 and CPD cells to SMC2. SMC2, a structural maintenance protein for chromosomes, is a component of the condensin complex, an important player in chromatin organization in the nucleus [101]. The images were acquired in 1x PBS solution like above. As shown in Fig 4-7 (b) and (d), both EPC2 and

CPD showed recognition signals for anti-SMC2 antibodies, which indicates the existence

of SMC2 proteins in our chromatin samples. Fig 4-7 (a) and Fig 4-7 (c) are the related

topography images.
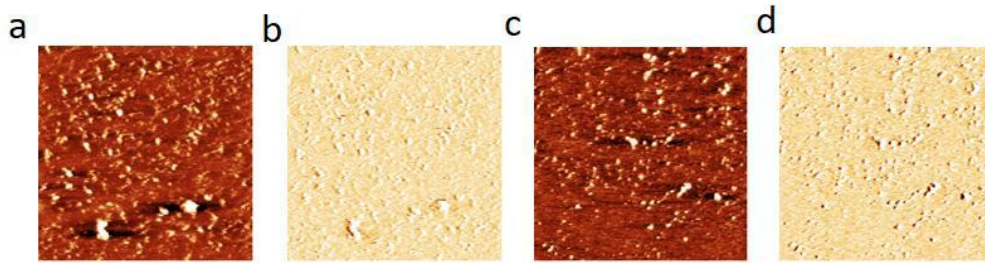
Fig 4-7. Topography and recognition images of EPC2 and CPD obtained with anti-SMC2 antibodies modified cantilevers. (a) and (b) are topography and recognition images for EPC2 chromatin samples. (c) and (d) are topography and recognition images for CPD chromatin samples. The size of each image is 1 μm x 1 μm.

Finally, the existence of histone H3 and SMC2 are also supported by western blotting

results. The chromatin extraction from the supernatant fraction of EPC2 and CPD were

used to in western blotting experiments. We found both histone H3 and SMC2 in both

EPC2 and CPD chromatin samples. The results are shown in Fig 4-8.
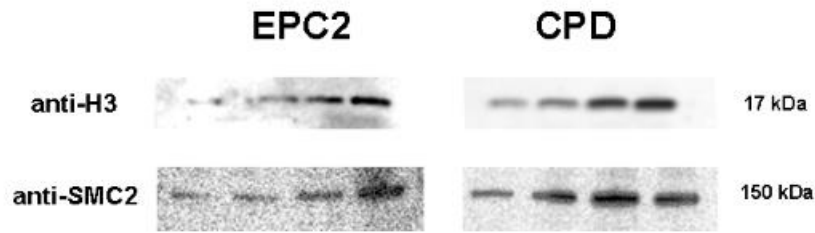
Fig 4-8. Western blotting of EPC2 and CP-D supernatant chromatin. The results confirmed the presence of histones H3 and SMC2 protein in the chromatin extraction. The left side is EPC2. The right side is CPD. The top two images are results for histone H3. A clear band at 17 kDa appears for both EPC2 and CPD supernatant chromatin. And the bottom two images show two bands at 150 kDa, which indicates the existence of SMC2 for both EPC2 and CPD supernatant chromatin.

4.4 Conclusions

Unlike previous studies using AFM recognition imaging on reconstituted chromatin, we successfully applied recognition imaging on native chromatin extracted from human cell lines. We found the existence of histones H3 and proteins SMC2 in our chromatin extraction. This will pave the way for analyzing the structures of chromatin from normal to cancerous human cells. The results from my research will help to get insights into the mechanisms of cell phenotype changes from normal to cancerous.

CHAPTER 5

CONTROLLED TRANSLOCATION OF DNA THROUGH SOLID STATE

NANOPORE

5.1 Introduction

The purpose of this research project is to control the DNA translocation speed through a nanopore for future sequencing of single glycosaminoglycan (GAG) molecules using recognition tunneling. GAGs are important components of the cell surface and the extracellular matrix (ECM) interface. They are linear acidic polysaccharides composed of repeating sulfated disaccharide units containing a uronic acid and a derivative of an amino sugar. There are two major types of GAGs. The first major type is heparan sulfate (HS) and heparin (HP). They contain glucosamine (GlcN) as the amino sugar and either glucuronic acid (GlcA) or iduronic acid (IdoA) as the uronic acid. Chondroitin sulfate (CS) is the second major type of GAGs. The amino sugar contained in CS is N-acetylgalactosamine (GalNAc) and GlcA is the uronic acid [102-105]. They are found in many organisms, including all mammals. The interactions between GAGs and numerous proteins at the cell-ECM interface modulate protein function and thus control fundamental biological processes. These include angiogenesis [106], regulatory functions in development [107], axonal growth [108], cancer progression [109] and so on. Despite these significant physiological applications, the structure-activity relationships between GAG sulfation patterns and their activity are still not fully understood. GAGs have large molecular weights. The biosynthesis of GAGs is non-template driven and several enzymes are involved [110, 111]. The complex biosynthesis and lack of regularity result in a large diversity of heterogeneous GAG structures. Each GAG is unique. Because of that, GAG

chains cannot be replicated or amplified like DNA. Homogeneous samples of intact GAGs are difficult, if not impossible to obtain. Thus, a single molecule technique may provide a unique way to elucidate the structures of individual GAG molecules.

A tunnel junction (a few nanometers apart) formed between two metal electrodes that is embedded in a solid-state nanopore had been used to sequence DNA, as shown in Fig 5-1. This method is called recognition tunneling (RT) and can result in the sequencing of GAGs. However, free GAGs will translocate through a nanopore too fast to resolve the sequence of GAGs by RT [23]. To achieve the goal of sequencing GAGs using the above-mentioned technique, slowing down the translocation speed of GAG molecules through the nanopore is crucial. GAG molecules can be linked to DNA. If we can control the translocation speed of DNA molecules, we can control the translocation speed of GAGs.
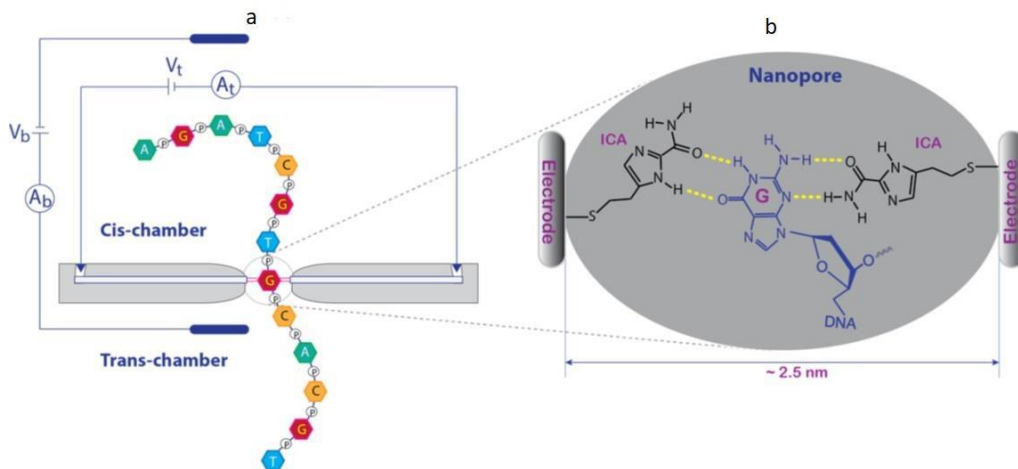
Fig 5-1. Schematic illustration of a tunneling junction and recognition tunneling. (a) A tunneling junction embedded in a nanopore used to sequence DNA. (b) indicates the mechanism of recognition tunneling. Both images are adapted from [112].

In 2009, Stoddart et al. proposed to discriminate single nucleotides in immobilized DNA oligonucleotides using a biological nanopore [113]. Recently, Wang et al. adopted edge-field leakage to slow down DNA translocation through a solid-state nanopore [114]. In our research, we used the characteristics of Φ29 polymerase to control DNA translocation speed. Φ29 polymerase is a member of the B-family of the replicative polymerases and has a molecular weight of 68 kDa. According to previous research, Φ29 polymerase can synthesize DNA molecules with a speed of one nucleotide every 10 ms [115]. That is, one DNA molecule can be elongated by about 0.3 nm every 10 ms. In our experiments, Φ29 molecules that are conjugated with a circular DNA template and a primer are deposited onto a silicon dioxide membrane containing a nanopore. The circular template is related to a technique called rolling-circle amplification (RCA) in which the polymerase can move along the template many rounds after one synthesis cycle is finished because the polymerase will reach the primer binding cite again at the end of the template. Single strand DNA (ssDNA) will be produced using this method. The schematic is shown in Fig 5-2. We were able to control the concentration of molecules for the surface modifications so that the nanopore is not blocked and there are enough Φ29 conjugates bound to the substrate close to the nanopore. First, unmodified primers were conjugated to Φ29 molecules. We added deoxyribonucleotide triphosphates (dNTPs) which are the building blocks of DNA to our nanopore related equipment after the substrates were functionalized with Φ29

59

conjugates. These dNTPs will be used to synthesize DNA (single strand DNA in our case) through the circular templates by Φ29. In contrast to typical micro-seconds uncontrolled single strand DNA translocation signals in nanopore experiments, we observed milli-seconds long or even longer translocation signals. These results are promising towards single GAG molecule sequencing.
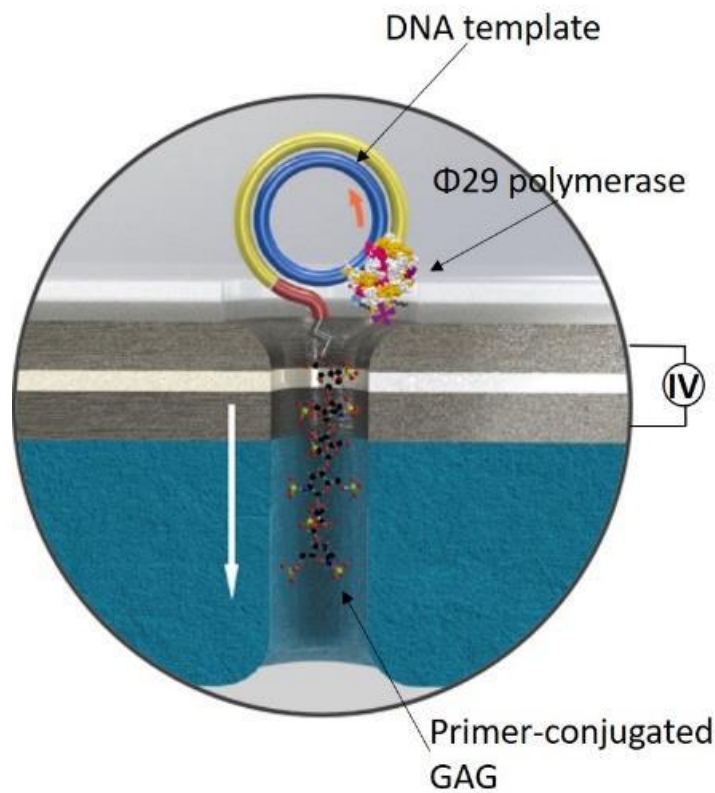
Fig 5-2. The mechanism behind controlled DNA movement through a nanopore using the RCA technique. A GAG conjugated to the polymerase, template and primer complex is also included in the image.

5.2 Materials and Methods

5.2.1 Solid-state Nanopores Fabrication

We used commercial solid-state chips from Norcada (NBPX5001Z-/OUO-HR, Norcada). The area of each chip is 5 mm x 5 mm. Each chip has a $200 \pm 10 \ \mu m$ thick silicon base. On top of the silicon base, there is one 12 ± 2 nm thick silicon nitride membrane. And a 5 nm thick silicon dioxide layer is grown on the silicon nitride membrane. Through etching technique, a 10 μm x 10 μm membrane window is made. Using transmission electron microscopy (2010F TEM from John M. Cowley Center for High Resolution Electron Microscopy (CHREM), ASU), a nanopore can be fabricated in the membrane window by focusing an electron beam on the membrane. Examples of a solid-state membrane and a solid-state nanopore can be seen in Fig 2-8.

5.2.2 Solid-state Membranes Functionalization and Imaging using AFM

To functionalize the membrane surface with a nanopore, the chip is cleaned in piranha solutions (3:1 H2SO4:H2O2) overnight. And then the chip is rinsed thoroughly with deionized water. Membrane surfaces were functionalized with 5 mg/mL siltrane-biotin (synthesized in our lab) solution by dropping 30 μL solutions to the surface for one hour. 25 μL 1 mg/mL streptavidin solution (N7021S, BioLabs) was incubated on the surface for one hour. In the end, 25 μL biotinylated Φ29 enzymes, circular template and primer complex solution were deposited on the surface for 40 minutes. In addition, we used two types of primers in our experiments. One was a normal unmodified primer, the other an aptamer modified primer (Fig. 5-3). After the surface was functionalized, the chip was glued to our nanopore setup [23]. And for the electrolytes, 1x reaction buffer (50 mM Tris, 10 mM MgCl2, 10 mM (NH4)2SO4, 4 mM DTT, pH 7.5) with 0.3 M KCl was filled in

both the top and bottom chambers of our instrument. In order to replicate DNA molecule using RCA during the experiment, 30 μL dNTP (N0447L, BioLabs) solution was added to the bottom chamber which has a volume of about 300 μL.
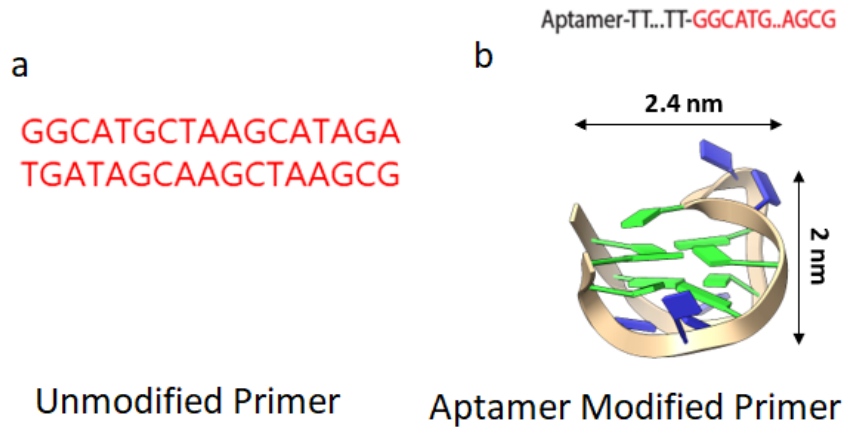
Fig 5-3. Two types of primers used in our experiments. (a) Unmodified primer sequence. (b) Aptamer modified primer with a representative image of an aptamer.

To get an idea about the enzyme coverage on the membrane after membrane functionalization, we imaged the membrane surface using Agilent 5500 AFM in tapping mode.

5.3 Results and Discussions

5.3.1 Controlled DNA Translocations with Unmodified Primers

In the first part of the experiments, unmodified primers were assembled with Φ29 enzyme and circular templates. After each step of functionalization of the membrane surface, an IV

curve was collected in order to see how currents vary under the same voltage. Typical IV curves for each step of functionalization are shown in Fig 5-4. After silatrane-biotin functionalization, the IV curve shows symmetric current sweeps. This might be because silatrane-biotin has no net charge at pH 7.5. The functionalization of siltrane-biotin is not affecting the movement of ions under an electric field. After streptavidin functionalization, no significant variations happened to the IV curve as well. The reason behind this is not clear to us yet. After the enzyme complex functionalization, we observed a flattening effect in the IV curve when negative voltage or small positive voltage were applied. That can be attributed to the highly positive net charge of Φ29 enzyme at pH 7.5.

Silatrane-biotin functionalization   Streptavidin functionalization   Enzyme functionalization
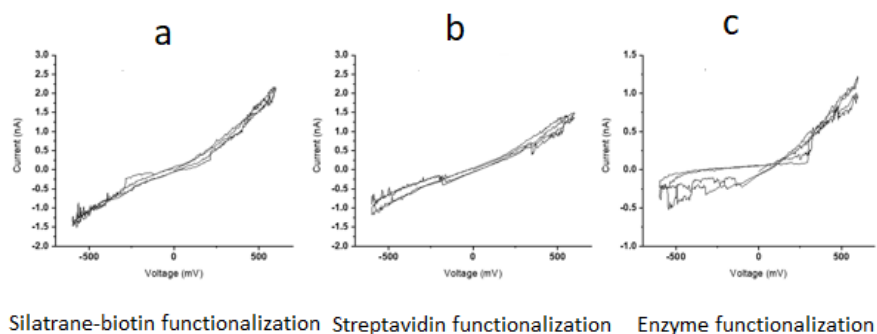
Fig 5-4. IV curves after each step of functionalization. (a) silatrane-biotin functionalization, (b) streptavidin functionalization and (c) Φ29 enzyme complex functionalization.

After checking the IV curves for each step of functionalization, we started collecting the ion current baseline until it stabilized before injecting dNTP into the *cis* chamber in order

to have a reference for translocation signals. After the addition of dNTP, we observed long

translocation signals (longer than 50 ms). Some of those signals are even longer than 10 s

as shown in Fig 5-5 a. This is different from sub-millisecond short translocations (see Fig

5-5 b). We hypothesize that long signals are related to controlled DNA translocations. A

DNA molecule is synthesized by one enzyme, circular template and primer complex while

it is moving through the nanopore under the electric field. We successfully obtained long

translocation signals for four separate experiments. However, only around 20 to 50 long

translocation signals were observed in each experimental run. Fig 5-6 shows the signal

(longer than 50 ms) dwell time distribution from one experiment. The small number of

long translocation signals might be because not many enzyme conjugates were located in

the vicinity of the nanopore considering the small dimension of the nanopore (usually the

nanopore has a diameter of about 3 nm). An AFM topography image that illustrates the

coverage of enzymes on the membrane is shown in Fig 5-7 (a). The size of one streptavidin

molecule is about 5 nm across and the size of one Φ29 enzyme, circular template and

primer complex is about 5 nm across as well. Silatrane-biotin molecules are smaller. Their

sizes are less than 2 nm across. We estimate the size of a full complex (one silatrane-biotin

molecule attached to the membrane surface, one streptavidin molecule bound to the

silatrane-biotin molecule and one biotinylated Φ29 enzyme bound to the streptavidin

molecule) to be around 11 nm high in the topography image. This number might vary a

little bit depending on the orientation of the molecules. We counted the particles with

height of about 11 nm within a $1\ \mu m^2$ area and found approximately 100 full complex

molecules. That means within a radial distance of 0.4 μm from the nanopore, there are

about 50 Φ29 enzymes immobilized. When DNA replication started under the activity of

these enzymes, the DNA molecules would be pulled by the electric field towards the nanopore. The DNA molecules (which we call rolling circle replication (RCR) products) replicated through our circular templates can reach 10 kb, which is $> 3 \ \mu m$. The electrophoresis results for these DNA molecules are shown in Fig 5-7 (c). Considering the activity of $\Phi 29$ enzymes, if a DNA molecule was pulled through the nanopore since the start of replication, it would take about 100 s for a 10 kb DNA molecule to translocate through the nanopore. Our observed times of 20s are below this upper limit. In addition, considering the stochasticity of biological processes, it is unrealistic for every enzyme that is immobilized in the vicinity of the nanopore to cause one long translocation signal. The small number (less than 50) of long translocation signals in one experiment can be explained by the fast electric field strength decreases away from the center of the nanopore. DNA molecules synthesized by enzyme conjugates far away from the nanopore cannot be pulled by the weak electric field through the nanopore while being synthesized. They will diffuse freely though the cell until they translocated though the nanopore resulting in the typical μs translocation times of free molecules. This might explain why we observed some short translocation signals in our experiments as well. Many synthesized DNA molecules will be released first and then diffuse towards to the nanopore. They will then be pulled by the electric field through the nanopore. These free DNA molecules can translocate through the nanopore fast and cause short translocation signals (see Fig 5-5 b).
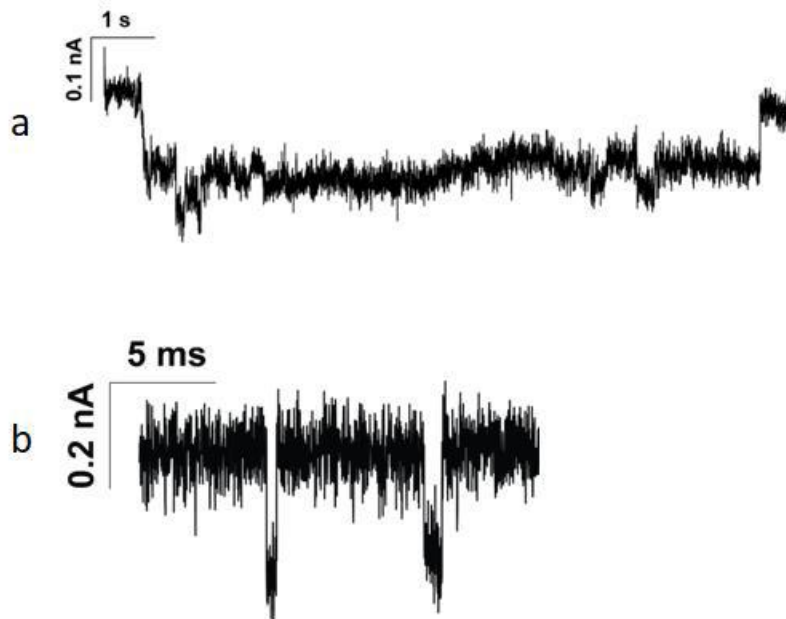
Fig 5-5. Translocation signals during experiments with unmodified primers. (a) A long translocation signal that is longer than 10 s. (b) Two short translocation signals that are in the sub-milliseconds range are shown.
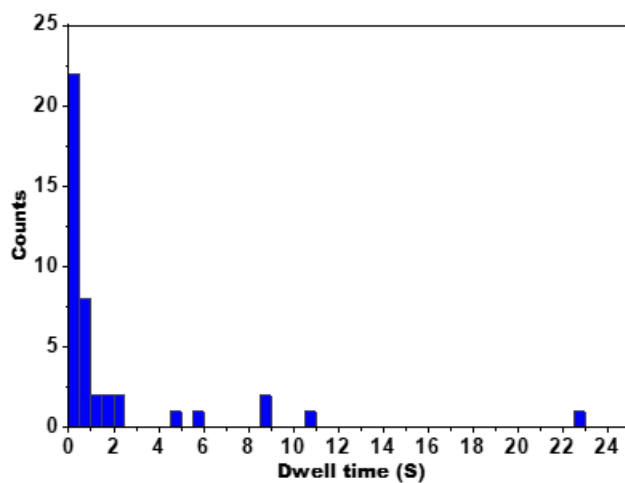
Fig 5-6. Long translocation signals dwell time distribution. For one experiment, we observed less than 50 long translocations signals.
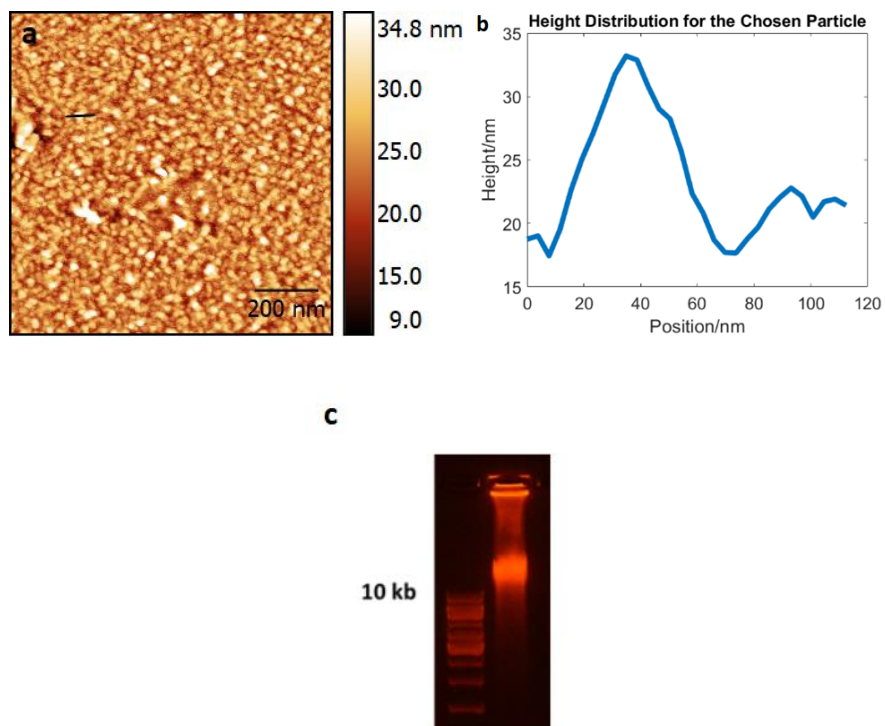
Fig 5-7. AFM topography image of Φ29 enzymes functionalized membrane and RCR products electrophoresis. (a) is the topography image of a membrane functionalized with Φ29 enzymes. (b) shows the height distribution of one chosen particle. (c) is the electrophoresis results for RCR products.

5.3.2 Uncontrolled Translocations of Free DNA Molecules

In order to confirm whether the long translocation signals are related to controlled DNA translocation or just because of the translocation of free DNA molecules through the nanopore, we produced similar ssDNA molecules using rolling circle replication (RCR). Then, we used unmodified membrane surfaces to conduct these control experiments to observe how these long DNA molecules translocate through the nanopores. As illustrated in Fig 5-8, the translocation signals are in the sub-milliseconds level.
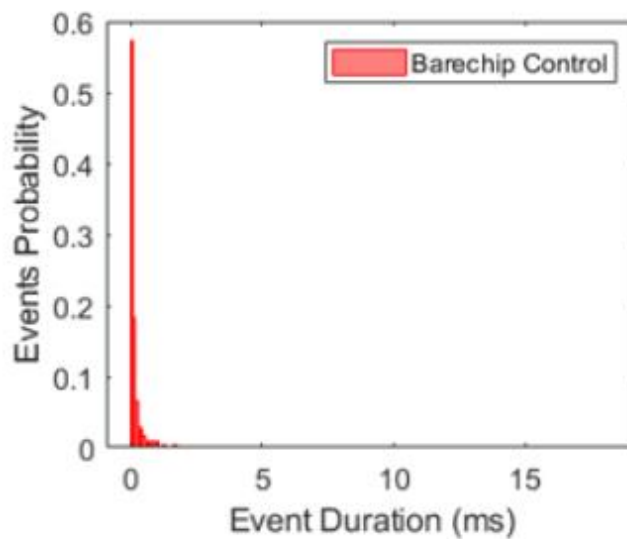
Fig 5-8. Free RCR products translocation signals distribution. The translocation signals distribution of free RCR products for one unmodified membrane surface is shown.

5.3.3 Controlled DNA Translocations with Aptamer Modified Primers

Until now, we haven't paid any attention to the blockade amplitude of the translocation signals. As one DNA molecule translocates through a nanopore, the molecule will exclude some volume of the nanopore decreasing the electrolytes flow through the nanopore. This will result in a decrease in ion current. To study how the size of one molecule is related to the amount of blocked ion current, a few parameters can be defined: the mean blocked-pore current $\langle ib \rangle$, and the dimensionless fractional current, $IB=\langle ib \rangle/\langle io \rangle$, where $\langle io \rangle$ is the open-pore current. According to the above definition, $1 - IB$ will be the blockade amplitude [116]. According to [116], $1 - IB = \left(\frac{a}{d}\right)^2$. In the equation, a is the cross-section dimension of the molecule translocating through the nanopore. And d is the diameter of the nanopore. With this equation in mind, we designed an experiment in which the primers are modified with aptamers so that when DNA molecules are synthesized by RCA, an aptamer will translocate through the nanopore first followed by single-strand DNA. For our aptamer structure, a is 2.4 nm as shown in Fig 5-3 b. While it is 1 nm for single-strand DNA molecules. Considering the thickness of our membrane (17 nm, with 12 nm silicon nitride and 5 nm silicon dioxide) and the synthesis speed of one nucleotide by one Φ29 enzyme (0.3 nm every 10 ms), we estimate to see a long translocation signal like Fig 5-9 a. In the beginning, one aptamer will translocate through the nanopore causing some ion currents blockade and the translocation duration time should be about 560 ms. It should be followed by a long translocation signal from ssDNA. However, considering the dimension of one aptamer molecule which is comparable to the dimension of our nanopores, the translocation duration time might be longer than 560 ms. In one of our experiments, we did see a signal as expected (Fig 5-9 b).

69

a

6 ΔI

Not short spike

ΔI

~ 560 ms for 17 nm
thick membrane

b

~ 1 s
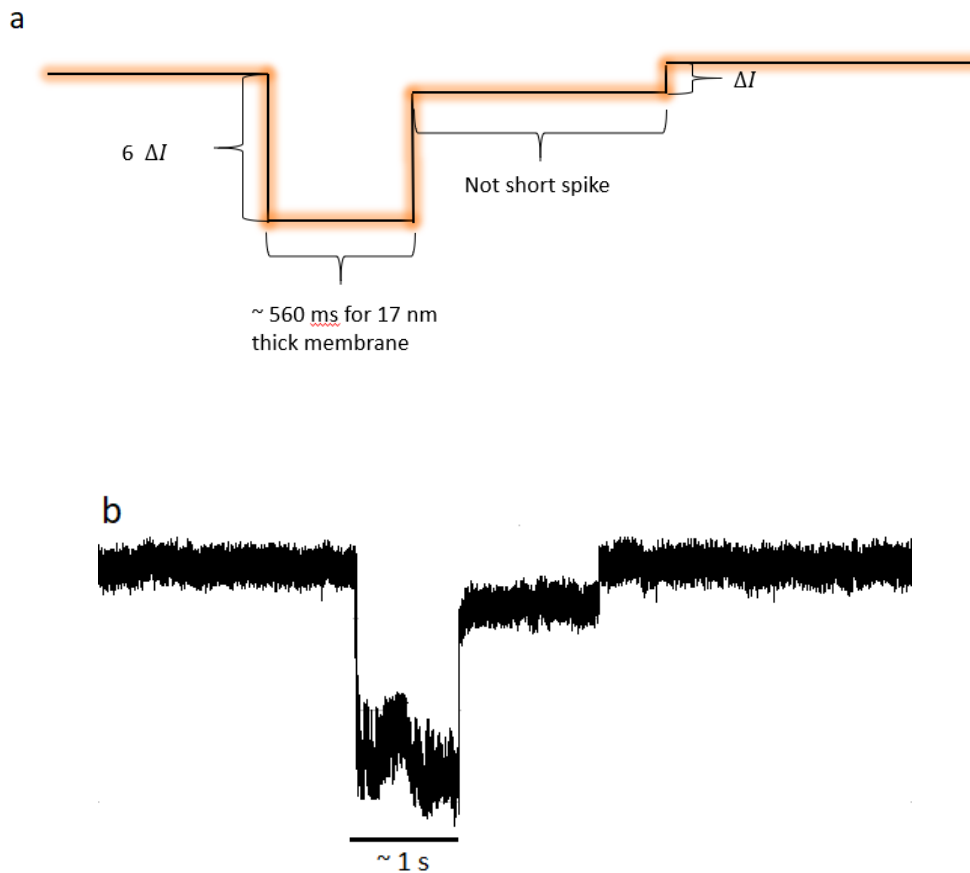
Fig 5-9. Expected and experimental data with aptamer modified primers. (a) This is the expected translocation signal for experiments with aptamer-modified primers. ΔI in the image represents the amount of ion currents blocked by a single strand DNA molecule. (b) In one of our experiments with aptamer-modified primers, we observed one long translocation signal. The first part of the long translocation signal lasts about 1 s which is consistent with our estimation for aptamer translocating through our 17 nm membrane. And the second part of the translocation signal lasts more than 1 s as well. The average blockade amplitude ratio for the two parts is about 6:1 which is consistent with our calculation according to the sizes of aptamer and single-strand DNA.

5.4 Conclusions

We found promising results for controlling the translocation of single DNA molecules through a nanopore. The controlled translocations of DNA molecules can be used to control the translocation speed of GAG molecules through a nanopore. This will help resolve single disaccharide units in a GAG molecule, which will improve our understanding of the structure-activities of GAG molecules in the near future.

CHAPTER 6

SUMMARY AND FUTURE STUDIES

This thesis contains various applications of AFM and nanopore translocation to biological systems, from single cells to single molecules.

In my first research project, AFM tapping mode imaging and KPFM techniques are applied to image a single *Salmonella typhimurium* cell, to characterize the surface roughness and surface potential of a single cell. The resolution of single cell surface image can reach a few nanometers. This provides us a good way to analyze the surface characteristics of a single *Salmonella typhimurium* cell locally as the surface of an intact *Salmonella typhimurium* cell is usually on the micrometer scale. Applying this methodology, the roughness and surface potential for different types of *Salmonella typhimurium* strains were obtained and compared. The analyses help us come up with the conclusion that *phoP* mutation will result in significant *Salmonella typhimurium* surface morphology and potential changes.

In addition, through applying AFM recognition imaging, chromatin extractions from normal (EPC2) and cancerous (CPD) esophageal cells were analyzed on the single molecule level. Histone H3 and protein SMC2 were successfully identified in both EPC2 and CPD chromatin extraction. Both amplitude blocking and peptide blocking helped reinstate this identification. Further, western blotting results support this as findings on the ensemble level. This will pave the way for analyzing the structures of chromatin from

normal to cancerous human cells. The results from my research will help to get insights into the mechanisms of cell phenotype changes from normal to cancerous.

My third research project focused on the controlled translocation of DNA through solid-state nanopores. Solid-state nanopores have several advantages comparing to biological nanopores. They are easy to reproduce, can stay active for a long time and can stand various harsh conditions. With the successful control of DNA translocation through solid-state nanopores, it will become possible to sequence a single GAG molecule combining the recognition tunneling technique. This will help resolve single disaccharide units in a GAG molecule, thus providing us with more detailed information about the different structures of different GAG molecules.

REFERENCES

[1]   H. Miller, Z. Zhou, J. Shepherd, A. J. M. Wollman, and M. C. Leake, "Single-molecule techniques in biophysics: a review of the progress in methods and applications," (in eng), *Rep Prog Phys,* vol. 81, no. 2, p. 024601, Feb 2018, doi: 10.1088/1361-6633/aa8a02.

[2]   O. L. Harriman and M. C. Leake, "Single molecule experimentation in biological physics: exploring the living component of soft condensed matter one molecule at a time," (in eng), *J Phys Condens Matter,* vol. 23, no. 50, p. 503101, Dec 21 2011, doi: 10.1088/0953-8984/23/50/503101.

[3]   F. Ritort, "Single-molecule experiments in biological physics: methods and applications," (in eng), *J Phys Condens Matter,* vol. 18, no. 32, pp. R531-83, Aug 16 2006, doi: 10.1088/0953-8984/18/32/r01.

[4]   A. A. Deniz, S. Mukhopadhyay, and E. A. Lemke, "Single-molecule biophysics: at the interface of biology, physics and chemistry," (in eng), *J R Soc Interface,* vol. 5, no. 18, pp. 15-45, Jan 6 2008, doi: 10.1098/rsif.2007.1021.

[5]   K. C. Neuman and A. Nagy, "Single-molecule force spectroscopy: optical tweezers, magnetic tweezers and atomic force microscopy," (in eng), *Nat Methods,* vol. 5, no. 6, pp. 491-505, Jun 2008, doi: 10.1038/nmeth.1218.

[6]   S. A. Claridge, J. J. Schwartz, and P. S. Weiss, "Electrons, photons, and force: quantitative single-molecule measurements from physics to biology," (in eng), *ACS Nano,* vol. 5, no. 2, pp. 693-729, Feb 22 2011, doi: 10.1021/nn103298x.

[7]   N. Jalili and K. Laxminarayana, "A review of atomic force microscopy imaging systems: application to molecular metrology and biological sciences," *Mechatronics,* vol. 14, no. 8, pp. 907-945, 2004/10/01/ 2004, doi: https://doi.org/10.1016/j.mechatronics.2004.04.005.

[8]   M. Krieg *et al.*, "Atomic force microscopy-based mechanobiology," *Nature Reviews Physics,* vol. 1, no. 1, pp. 41-57, 2019/01/01 2019, doi: 10.1038/s42254-018-0001-7.

[9]   D. P. Allison, N. P. Mortensen, C. J. Sullivan, and M. J. Doktycz, "Atomic force microscopy of biological samples," (in eng), *Wiley Interdiscip Rev Nanomed Nanobiotechnol,* vol. 2, no. 6, pp. 618-34, Nov-Dec 2010, doi: 10.1002/wnan.104.

[10]   A. Loyola-Leyva, J. P. Loyola-Rodríguez, M. Atzori, and F. J. González, "Morphological changes in erythrocytes of people with type 2 diabetes mellitus evaluated with atomic force microscopy: A brief review," (in eng), *Micron,* vol. 105, pp. 11-17, Feb 2018, doi: 10.1016/j.micron.2017.11.001.

[11]   S. Vahabi, B. Nazemi Salman, and A. Javanmard, "Atomic force microscopy application in biological research: a review study," (in eng), *Iranian journal of medical sciences,* vol. 38, no. 2, pp. 76-83, 2013.

[12]   P.-H. Wu *et al.*, "A comparison of methods to assess cell mechanical properties," *Nature Methods,* vol. 15, no. 7, pp. 491-498, 2018/07/01 2018, doi: 10.1038/s41592-018-0015-1.

[13]   N. Peela *et al.*, "A three dimensional micropatterned tumor model for breast cancer cell migration studies," *Biomaterials,* vol. 81, pp. 72-83, 2016/03/01/ 2016, doi: https://doi.org/10.1016/j.biomaterials.2015.11.039.

[14]   D. Deamer, M. Akeson, and D. Branton, "Three decades of nanopore sequencing," *Nature biotechnology,* vol. 34, no. 5, pp. 518-524, 2016.

[15]   D. Branton *et al.*, "The potential and challenges of nanopore sequencing," *Nature biotechnology,* vol. 26, no. 10, pp. 1146-1153, 2008.

[16]   M. Wanunu, "Nanopores: A journey towards DNA sequencing," (in eng), *Phys Life Rev,* vol. 9, no. 2, pp. 125-58, Jun 2012, doi: 10.1016/j.plrev.2012.05.010.

[17]   M. Akeson, D. Branton, J. J. Kasianowicz, E. Brandin, and D. W. Deamer, "Microsecond Time-Scale Discrimination Among Polycytidylic Acid, Polyadenylic Acid, and Polyuridylic Acid as Homopolymers or as Segments Within Single RNA Molecules," *Biophysical Journal,* vol. 77, no. 6, pp. 3227-3233, 1999/12/01/ 1999, doi: https://doi.org/10.1016/S0006-3495(99)77153-5.

[18]   E. A. Manrao *et al.*, "Reading DNA at single-nucleotide resolution with a mutant MspA nanopore and phi29 DNA polymerase," *Nature Biotechnology,* vol. 30, no. 4, pp. 349-353, 2012/04/01 2012, doi: 10.1038/nbt.2171.

[19]   H. Bayley, "Sequencing single molecules of DNA," *Current Opinion in Chemical Biology,* vol. 10, no. 6, pp. 628-637, 2006/12/01/ 2006, doi: https://doi.org/10.1016/j.cbpa.2006.10.040.

[20]   P. D. Tamma, S. E. Cosgrove, and L. L. Maragakis, "Combination therapy for treatment of infections with gram-negative bacteria," *Clinical microbiology reviews,* vol. 25, no. 3, pp. 450-470, 2012.

[21] H. Wright, R. A. Bonomo, and D. L. Paterson, "New agents for the treatment of infections with Gram-negative bacteria: restoring the miracle or false dawn?," *Clinical Microbiology and Infection,* vol. 23, no. 10, pp. 704-712, 2017.

[22] A. Y. Peleg and D. C. Hooper, "Hospital-acquired infections due to gram-negative bacteria," *New England Journal of Medicine,* vol. 362, no. 19, pp. 1804-1813, 2010.

[23] J. Im, S. Lindsay, X. Wang, and P. Zhang, "Single Molecule Identification and Quantification of Glycosaminoglycans Using Solid-State Nanopores," (in eng), *ACS Nano,* vol. 13, no. 6, pp. 6308-6318, Jun 25 2019, doi: 10.1021/acsnano.9b00618.

[24] T. J. Beveridge and J. A. Davies, "Cellular responses of Bacillus subtilis and Escherichia coli to the Gram stain," (in eng), *J Bacteriol,* vol. 156, no. 2, pp. 846-58, Nov 1983, doi: 10.1128/jb.156.2.846-858.1983.

[25] R. Coico, "Gram staining," (in eng), *Curr Protoc Microbiol,* vol. Appendix 3, p. Appendix 3C, Oct 2005, doi: 10.1002/9780471729259.mca03cs00.

[26] A. Farhana and Y. S. Khan, "Biochemistry, Lipopolysaccharide," in *StatPearls*. Treasure Island (FL): StatPearls Publishing Copyright © 2022, StatPearls Publishing LLC., 2022.

[27] T. J. Silhavy, D. Kahne, and S. Walker, "The bacterial cell envelope," (in eng), *Cold Spring Harb Perspect Biol,* vol. 2, no. 5, p. a000414, May 2010, doi: 10.1101/cshperspect.a000414.

[28] P. Sperandeo, A. M. Martorana, and A. Polissi, "Lipopolysaccharide Biosynthesis and Transport to the Outer Membrane of Gram-Negative Bacteria," (in eng), *Subcell Biochem,* vol. 92, pp. 9-37, 2019, doi: 10.1007/978-3-030-18768-2_2.

[29] I. C. Sutcliffe, "A phylum level perspective on bacterial cell envelope architecture," (in eng), *Trends Microbiol,* vol. 18, no. 10, pp. 464-70, Oct 2010, doi: 10.1016/j.tim.2010.06.005.

[30] G. Binnig, C. F. Quate, and C. Gerber, "Atomic force microscope," (in eng), *Phys Rev Lett,* vol. 56, no. 9, pp. 930-933, Mar 3 1986, doi: 10.1103/PhysRevLett.56.930.

[31] D. Alsteens, H. E. Gaub, R. Newton, M. Pfreundschuh, C. Gerber, and D. J. Müller, "Atomic force microscopy-based characterization and design of biointerfaces," *Nature Reviews Materials,* vol. 2, no. 5, pp. 1-16, 2017.

[32]   M. Lanza, *Conductive Atomic Force Microscopy: Applications in Nanomaterials*. John Wiley & Sons, 2017.

[33]   B. J. Rodriguez and S. V. Kalinin, "KPFM and PFM of Biological Systems," in *Kelvin Probe Force Microscopy: Measuring and Compensating Electrostatic Forces*, S. Sadewasser and T. Glatzel Eds. Berlin, Heidelberg: Springer Berlin Heidelberg, 2012, pp. 243-287.

[34]   I. Casuso *et al.*, "Electron transport through supported biomembranes at the nanoscale by conductive atomic force microscopy," *Nanotechnology,* vol. 18, no. 46, p. 465503, 2007.

[35]   Y. Martin, C. C. Williams, and H. K. Wickramasinghe, "Atomic force microscope–force mapping and profiling on a sub 100-Å scale," *Journal of Applied Physics,* vol. 61, no. 10, pp. 4723-4729, 1987/05/15 1987, doi: 10.1063/1.338807.

[36]   Q. Zhong, D. Inniss, K. Kjoller, and V. B. Elings, "Fractured polymer/silica fiber surface studied by tapping mode atomic force microscopy," *Surface Science Letters,* vol. 290, no. 1, pp. L688-L692, 1993/06/10/ 1993, doi: https://doi.org/10.1016/0167-2584(93)90906-Y.

[37]   A. Raab *et al.*, "Antibody recognition imaging by force microscopy," (in eng), *Nat Biotechnol,* vol. 17, no. 9, pp. 901-5, Sep 1999, doi: 10.1038/12898.

[38]   C. Stroh *et al.*, "Single-molecule recognition imaging microscopy," (in eng), *Proc Natl Acad Sci U S A,* vol. 101, no. 34, pp. 12503-7, Aug 24 2004, doi: 10.1073/pnas.0403538101.

[39]   A. Ebner *et al.*, "Localization of single avidin-biotin interactions using simultaneous topography and molecular recognition imaging," (in eng), *Chemphyschem,* vol. 6, no. 5, pp. 897-900, May 2005, doi: 10.1002/cphc.200400545.

[40]   H. Wang, R. Bash, S. M. Lindsay, and D. Lohr, "Solution AFM studies of human Swi-Snf and its interactions with MMTV DNA and chromatin," (in eng), *Biophys J,* vol. 89, no. 5, pp. 3386-98, Nov 2005, doi: 10.1529/biophysj.105.065391.

[41]   H. Wang, Y. Dalal, S. Henikoff, and S. Lindsay, "Single-epitope recognition imaging of native chromatin," (in eng), *Epigenetics Chromatin,* vol. 1, no. 1, p. 10, Dec 17 2008, doi: 10.1186/1756-8935-1-10.

[42]   W. H. Coulter, "US Patent No. 2,656,508," *Appl. 27August1949. Publ. 20October1953,* 1953.

[43] R. W. DeBlois, C. P. Bean, and R. K. A. Wesley, "Electrokinetic measurements with submicron particles and pores by the resistive pulse technique," *Journal of Colloid and Interface Science,* vol. 61, no. 2, pp. 323-335, 1977/09/01/ 1977, doi: https://doi.org/10.1016/0021-9797(77)90395-2.

[44] L. Song, M. R. Hobaugh, C. Shustak, S. Cheley, H. Bayley, and J. E. Gouaux, "Structure of staphylococcal alpha-hemolysin, a heptameric transmembrane pore," (in eng), *Science,* vol. 274, no. 5294, pp. 1859-66, Dec 13 1996, doi: 10.1126/science.274.5294.1859.

[45] T. Z. Butler, M. Pavlenok, I. M. Derrington, M. Niederweis, and J. H. Gundlach, "Single-molecule DNA detection with an engineered MspA protein nanopore," (in eng), *Proc Natl Acad Sci U S A,* vol. 105, no. 52, pp. 20647-52, Dec 30 2008, doi: 10.1073/pnas.0807514106.

[46] D. Wendell *et al.*, "Translocation of double-stranded DNA through membrane-adapted phi29 motor protein nanopores," (in eng), *Nat Nanotechnol,* vol. 4, no. 11, pp. 765-72, Nov 2009, doi: 10.1038/nnano.2009.259.

[47] D. C. Harris, *Quantitative chemical analysis*. Macmillan, 2010.

[48] M. J. Kim, M. Wanunu, D. C. Bell, and A. Meller, "Rapid fabrication of uniformly sized nanopores and nanopore arrays for parallel DNA analysis," *Advanced materials,* vol. 18, no. 23, pp. 3149-3153, 2006.

[49] R. M. M. Smeets, U. F. Keyser, D. Krapf, M.-Y. Wu, N. H. Dekker, and C. Dekker, "Salt dependence of ion transport and DNA translocation through solid-state nanopores," *Nano letters,* vol. 6, no. 1, pp. 89-95, 2006.

[50] F. H. J. van der Heyden, D. Stein, and C. Dekker, "Streaming currents in a single nanofluidic channel," *Physical review letters,* vol. 95, no. 11, p. 116104, 2005.

[51] K. Luger, A. W. Mäder, R. K. Richmond, D. F. Sargent, and T. J. Richmond, "Crystal structure of the nucleosome core particle at 2.8 A resolution," (in eng), *Nature,* vol. 389, no. 6648, pp. 251-60, Sep 18 1997, doi: 10.1038/38444.

[52] J. Bednar *et al.*, "Nucleosomes, linker DNA, and linker histone form a unique structural motif that directs the higher-order folding and compaction of chromatin," (in eng), *Proc Natl Acad Sci U S A,* vol. 95, no. 24, pp. 14173-8, Nov 24 1998, doi: 10.1073/pnas.95.24.14173.

[53] W. An, S. H. Leuba, K. van Holde, and J. Zlatanova, "Linker histone protects linker DNA on only one side of the core particle and in a sequence-dependent manner," (in eng), *Proc Natl Acad Sci U S A,* vol. 95, no. 7, pp. 3396-401, Mar 31 1998, doi: 10.1073/pnas.95.7.3396.

[54]   G. Felsenfeld and M. Groudine, "Controlling the double helix," (in eng), *Nature,* vol. 421, no. 6921, pp. 448-53, Jan 23 2003, doi: 10.1038/nature01411.

[55]   R. P. McCord, N. Kaplan, and L. Giorgetti, "Chromosome Conformation Capture and Beyond: Toward an Integrative View of Chromosome Structure and Function," (in eng), *Mol Cell,* vol. 77, no. 4, pp. 688-708, Feb 20 2020, doi: 10.1016/j.molcel.2019.12.021.

[56]   A. Bolzer *et al.*, "Three-dimensional maps of all chromosomes in human male fibroblast nuclei and prometaphase rosettes," (in eng), *PLoS Biol,* vol. 3, no. 5, p. e157, May 2005, doi: 10.1371/journal.pbio.0030157.

[57]   T. Cremer and C. Cremer, "Chromosome territories, nuclear architecture and gene regulation in mammalian cells," (in eng), *Nat Rev Genet,* vol. 2, no. 4, pp. 292-301, Apr 2001, doi: 10.1038/35066075.

[58]   J. Dekker, K. Rippe, M. Dekker, and N. Kleckner, "Capturing chromosome conformation," (in eng), *Science,* vol. 295, no. 5558, pp. 1306-11, Feb 15 2002, doi: 10.1126/science.1067799.

[59]   Z. Zhao *et al.*, "Circular chromosome conformation capture (4C) uncovers extensive networks of epigenetically regulated intra- and interchromosomal interactions," (in eng), *Nat Genet,* vol. 38, no. 11, pp. 1341-7, Nov 2006, doi: 10.1038/ng1891.

[60]   J. Dostie *et al.*, "Chromosome Conformation Capture Carbon Copy (5C): a massively parallel solution for mapping interactions between genomic elements," (in eng), *Genome Res,* vol. 16, no. 10, pp. 1299-309, Oct 2006, doi: 10.1101/gr.5571506.

[61]   E. Lieberman-Aiden *et al.*, "Comprehensive mapping of long-range interactions reveals folding principles of the human genome," (in eng), *Science,* vol. 326, no. 5950, pp. 289-93, Oct 9 2009, doi: 10.1126/science.1181369.

[62]   Y. Zhan *et al.*, "Reciprocal insulation analysis of Hi-C data shows that TADs represent a functionally but not structurally privileged scale in the hierarchical folding of chromosomes," (in eng), *Genome Res,* vol. 27, no. 3, pp. 479-490, Mar 2017, doi: 10.1101/gr.212803.116.

[63]   E. de Wit *et al.*, "CTCF Binding Polarity Determines Chromatin Looping," (in eng), *Mol Cell,* vol. 60, no. 4, pp. 676-84, Nov 19 2015, doi: 10.1016/j.molcel.2015.09.023.

[64] Y. Guo *et al.*, "CRISPR Inversion of CTCF Sites Alters Genome Topology and Enhancer/Promoter Function," (in eng), *Cell,* vol. 162, no. 4, pp. 900-10, Aug 13 2015, doi: 10.1016/j.cell.2015.07.038.

[65] L. Vian *et al.*, "The Energetics and Physiological Impact of Cohesin Extrusion," (in eng), *Cell,* vol. 173, no. 5, pp. 1165-1178.e20, May 17 2018, doi: 10.1016/j.cell.2018.03.072.

[66] L. Lin *et al.*, "Recognition imaging of acetylated chromatin using a DNA aptamer," (in eng), *Biophys J,* vol. 97, no. 6, pp. 1804-7, Sep 16 2009, doi: 10.1016/j.bpj.2009.06.045.

[67] H. Nikaido, "Molecular basis of bacterial outer membrane permeability revisited," (in eng), *Microbiol Mol Biol Rev,* vol. 67, no. 4, pp. 593-656, Dec 2003, doi: 10.1128/mmbr.67.4.593-656.2003.

[68] G. Zhang, T. C. Meredith, and D. Kahne, "On the essentiality of lipopolysaccharide to Gram-negative bacteria," (in eng), *Current opinion in microbiology,* vol. 16, no. 6, pp. 779-785, 2013, doi: 10.1016/j.mib.2013.09.007.

[69] R. E. Bishop, "Structural biology of membrane-intrinsic beta-barrel enzymes: sentinels of the bacterial outer membrane," (in eng), *Biochim Biophys Acta,* vol. 1778, no. 9, pp. 1881-96, Sep 2008, doi: 10.1016/j.bbamem.2007.07.021.

[70] T. S. Carpenter, J. Parkin, and S. Khalid, "The Free Energy of Small Solute Permeation through the Escherichia coli Outer Membrane Has a Distinctly Asymmetric Profile," (in eng), *J Phys Chem Lett,* vol. 7, no. 17, pp. 3446-51, Sep 1 2016, doi: 10.1021/acs.jpclett.6b01399.

[71] I. M. Helander, I. Kilpeläinen, and M. Vaara, "Increased substitution of phosphate groups in lipopolysaccharides and lipid A of the polymyxin-resistant pmrA mutants of Salmonella typhimurium: a 31P-NMR study," *Molecular Microbiology,* https://doi.org/10.1111/j.1365-2958.1994.tb00329.x vol. 11, no. 3, pp. 481-487, 1994/02/01 1994, doi: https://doi.org/10.1111/j.1365-2958.1994.tb00329.x.

[72] J. Jantsch, D. Chikkaballi, and M. Hensel, "Cellular aspects of immunity to intracellular Salmonella enterica," (in eng), *Immunol Rev,* vol. 240, no. 1, pp. 185-95, Mar 2011, doi: 10.1111/j.1600-065X.2010.00981.x.

[73] W. Rabsch *et al.*, "Salmonella enterica serotype Typhimurium and its host-adapted variants," (in eng), *Infection and immunity,* vol. 70, no. 5, pp. 2249-2255, 2002, doi: 10.1128/IAI.70.5.2249-2255.2002.

[74]   E. A. Groisman, C. Parra-Lopez, M. Salcedo, C. J. Lipps, and F. Heffron, "Resistance to host antimicrobial peptides is necessary for Salmonella virulence," (in eng), *Proc Natl Acad Sci U S A,* vol. 89, no. 24, pp. 11939-43, Dec 15 1992, doi: 10.1073/pnas.89.24.11939.

[75]   E. A. Groisman, E. Chiao, C. J. Lipps, and F. Heffron, "Salmonella typhimurium phoP virulence gene is a transcriptional regulator," (in eng), *Proc Natl Acad Sci U S A,* vol. 86, no. 18, pp. 7077-81, Sep 1989, doi: 10.1073/pnas.86.18.7077.

[76]   R. E. Bishop, H. S. Gibbons, T. Guina, M. S. Trent, S. I. Miller, and C. R. Raetz, "Transfer of palmitate from phospholipids to lipid A in outer membranes of gram-negative bacteria," (in eng), *Embo j,* vol. 19, no. 19, pp. 5071-80, Oct 2 2000, doi: 10.1093/emboj/19.19.5071.

[77]   E. García Véscovi, F. C. Soncini, and E. A. Groisman, "Mg2+ as an extracellular signal: environmental regulation of Salmonella virulence," (in eng), *Cell,* vol. 84, no. 1, pp. 165-74, Jan 12 1996, doi: 10.1016/s0092-8674(00)81003-x.

[78]   A. Kato, H. Tanabe, and R. Utsumi, "Molecular characterization of the PhoP-PhoQ two-component system in Escherichia coli K-12: identification of extracellular Mg2+-responsive promoters," (in eng), *J Bacteriol,* vol. 181, no. 17, pp. 5516-20, Sep 1999, doi: 10.1128/jb.181.17.5516-5520.1999.

[79]   D. Alsteens, A. Beaussart, S. El-Kirat-Chatel, R. M. Sullan, and Y. F. Dufrêne, "Atomic force microscopy: a new look at pathogens," (in eng), *PLoS Pathog,* vol. 9, no. 9, p. e1003516, 2013, doi: 10.1371/journal.ppat.1003516.

[80]   G. Andre *et al.*, "Imaging the nanoscale organization of peptidoglycan in living Lactococcus lactis cells," (in eng), *Nat Commun,* vol. 1, no. 3, p. 27, Jun 15 2010, doi: 10.1038/ncomms1027.

[81]   G. Francius *et al.*, "Detection, localization, and conformational analysis of single polysaccharide molecules on live bacteria," (in eng), *ACS Nano,* vol. 2, no. 9, pp. 1921-9, Sep 23 2008, doi: 10.1021/nn800341b.

[82]   G. Andre *et al.*, "Fluorescence and atomic force microscopy imaging of wall teichoic acids in Lactobacillus plantarum," (in eng), *ACS Chem Biol,* vol. 6, no. 4, pp. 366-76, Apr 15 2011, doi: 10.1021/cb1003509.

[83]   E. J. Hayhurst, L. Kailas, J. K. Hobbs, and S. J. Foster, "Cell wall peptidoglycan architecture in Bacillus subtilis," (in eng), *Proc Natl Acad Sci U S A,* vol. 105, no. 38, pp. 14603-8, Sep 23 2008, doi: 10.1073/pnas.0804138105.

[84]   A. Umeda, M. Saito, and K. Amako, "Surface characteristics of gram‑negative and gram‑positive bacteria in an atomic force microscope image," *Microbiology and immunology,* vol. 42, no. 3, pp. 159-164, 1998.

[85]   E. Birkenhauer and S. Neethirajan, "Surface potential measurement of bacteria using Kelvin probe force microscopy," (in eng), *J Vis Exp,* no. 93, p. e52327, Nov 28 2014, doi: 10.3791/52327.

[86]   Y. Shi, M. J. Cromie, F. F. Hsu, J. Turk, and E. A. Groisman, "PhoP-regulated Salmonella resistance to the antimicrobial peptides magainin 2 and polymyxin B," (in eng), *Mol Microbiol,* vol. 53, no. 1, pp. 229-41, Jul 2004, doi: 10.1111/j.1365-2958.2004.04107.x.

[87]   M. Raposo, Q. Ferreira, and P. A. Ribeiro, "A guide for atomic force microscopy analysis of soft-condensed matter," *Modern research and educational topics in microscopy,* vol. 1, pp. 758-769, 2007.

[88]   P. J. Cumpson, C. A. Clifford, and J. Hedley, "Quantitative analytical atomic force microscopy: a cantilever reference device for easy and accurate AFM spring-constant calibration," *Measurement Science and Technology,* vol. 15, no. 7, pp. 1337-1346, 2004/06/17 2004, doi: 10.1088/0957-0233/15/7/016.

[89]   L. Leive, "The barrier function of the gram-negative envelope," (in eng), *Ann N Y Acad Sci,* vol. 235, no. 0, pp. 109-29, May 10 1974, doi: 10.1111/j.1749-6632.1974.tb43261.x.

[90]   L. Guo *et al.*, "Regulation of lipid A modifications by Salmonella typhimurium virulence genes phoP-phoQ," (in eng), *Science,* vol. 276, no. 5310, pp. 250-3, Apr 11 1997, doi: 10.1126/science.276.5310.250.

[91]   L. Guo *et al.*, "Lipid A acylation and bacterial resistance against vertebrate antimicrobial peptides," (in eng), *Cell,* vol. 95, no. 2, pp. 189-98, Oct 16 1998, doi: 10.1016/s0092-8674(00)81750-x.

[92]   J. W. Lichtman and J. A. Conchello, "Fluorescence microscopy," (in eng), *Nat Methods,* vol. 2, no. 12, pp. 910-9, Dec 2005, doi: 10.1038/nmeth817.

[93]   A. Ashkin, "Forces of a single-beam gradient laser trap on a dielectric sphere in the ray optics regime," (in eng), *Biophys J,* vol. 61, no. 2, pp. 569-82, Feb 1992, doi: 10.1016/s0006-3495(92)81860-x.

[94]   M. L. Bennink, S. H. Leuba, G. H. Leno, J. Zlatanova, B. G. de Grooth, and J. Greve, "Unfolding individual nucleosomes by stretching single chromatin fibers with optical tweezers," *Nature structural biology,* vol. 8, no. 7, pp. 606-610, 2001.

[95]   W. Kalle and P. Strappe, "Atomic force microscopy on chromosomes, chromatin and DNA: A review," *Micron,* vol. 43, no. 12, pp. 1224-1231, 2012/12/01/ 2012, doi: https://doi.org/10.1016/j.micron.2012.04.004.

[96]   M. M. Sanders, "Fractionation of nucleosomes by salt elution from micrococcal nuclease-digested nuclei," *The Journal of cell biology,* vol. 79, no. 1, pp. 97-109, 1978.

[97]   H. Wang, L. Obenauer-Kutner, M. Lin, Y. Huang, M. J. Grace, and S. M. Lindsay, "Imaging glycosylation," (in eng), *J Am Chem Soc,* vol. 130, no. 26, pp. 8154-5, Jul 2 2008, doi: 10.1021/ja802535p.

[98]   D. Lohr, R. Bash, H. Wang, J. Yodh, and S. Lindsay, "Using atomic force microscopy to study chromatin structure and nucleosome remodeling," (in eng), *Methods,* vol. 41, no. 3, pp. 333-41, Mar 2007, doi: 10.1016/j.ymeth.2006.08.016.

[99]   H. Wang, R. Bash, J. G. Yodh, G. Hager, S. M. Lindsay, and D. Lohr, "Using atomic force microscopy to study nucleosome remodeling on individual nucleosomal arrays in situ," (in eng), *Biophys J,* vol. 87, no. 3, pp. 1964-71, Sep 2004, doi: 10.1529/biophysj.104.042606.

[100] L. A. Chtcheglova and P. Hinterdorfer, "Simultaneous AFM topography and recognition imaging at the plasma membrane of mammalian cells," (in eng), *Semin Cell Dev Biol,* vol. 73, pp. 45-56, Jan 2018, doi: 10.1016/j.semcdb.2017.08.025.

[101] M. S. van Ruiten and B. D. Rowland, "SMC Complexes: Universal DNA Looping Machines with Distinct Regulators," (in eng), *Trends Genet,* vol. 34, no. 6, pp. 477-487, Jun 2018, doi: 10.1016/j.tig.2018.03.003.

[102] R. Sasisekharan, R. Raman, and V. Prabhakar, "Glycomics approach to structure-function relationships of glycosaminoglycans," (in eng), *Annu Rev Biomed Eng,* vol. 8, pp. 181-231, 2006, doi: 10.1146/annurev.bioeng.8.061505.095745.

[103] J. R. Bishop, M. Schuksz, and J. D. Esko, "Heparan sulphate proteoglycans fine-tune mammalian physiology," (in eng), *Nature,* vol. 446, no. 7139, pp. 1030-7, Apr 26 2007, doi: 10.1038/nature05817.

[104] U. Lindahl and J. P. Li, "Interactions between heparan sulfate and proteins-design and functional implications," (in eng), *Int Rev Cell Mol Biol,* vol. 276, pp. 105-59, 2009, doi: 10.1016/s1937-6448(09)76003-4.

[105] P. L. DeAngelis, "Evolution of glycosaminoglycans and their glycosyltransferases: Implications for the extracellular matrices of animals and

the capsules of pathogenic bacteria," (in eng), *Anat Rec,* vol. 268, no. 3, pp. 317-26, Nov 1 2002, doi: 10.1002/ar.10163.

[106] B. Casu *et al.*, "Short heparin sequences spaced by glycol-split uronate residues are antagonists of fibroblast growth factor 2 and angiogenesis inhibitors," (in eng), *Biochemistry,* vol. 41, no. 33, pp. 10519-28, Aug 20 2002, doi: 10.1021/bi020118n.

[107] G. K. Dhoot, M. K. Gustafsson, X. Ai, W. Sun, D. M. Standiford, and C. P. Emerson, Jr., "Regulation of Wnt signaling and embryo patterning by an extracellular sulfatase," (in eng), *Science,* vol. 293, no. 5535, pp. 1663-6, Aug 31 2001, doi: 10.1126/science.293.5535.1663.

[108] L. I. Benowitz, D. E. Goldberg, and N. Irwin, "Inosine stimulates axon growth in vitro and in the adult CNS," (in eng), *Prog Brain Res,* vol. 137, pp. 389-99, 2002, doi: 10.1016/s0079-6123(02)37030-4.

[109] K. Sugahara, T. Mikami, T. Uyama, S. Mizuguchi, K. Nomura, and H. Kitagawa, "Recent advances in the structural biology of chondroitin sulfate and dermatan sulfate," (in eng), *Curr Opin Struct Biol,* vol. 13, no. 5, pp. 612-20, Oct 2003, doi: 10.1016/j.sbi.2003.09.011.

[110] K. Sugahara and H. Kitagawa, "Heparin and heparan sulfate biosynthesis," (in eng), *IUBMB Life,* vol. 54, no. 4, pp. 163-75, Oct 2002, doi: 10.1080/15216540214928.

[111] M. Kusche-Gullberg and L. Kjellén, "Sulfotransferases in glycosaminoglycan biosynthesis," (in eng), *Curr Opin Struct Biol,* vol. 13, no. 5, pp. 605-11, Oct 2003, doi: 10.1016/j.sbi.2003.08.002.

[112] S. Biswas *et al.*, "Universal Readers Based on Hydrogen Bonding or π–π Stacking for Identification of DNA Nucleotides in Electron Tunnel Junctions," *ACS Nano,* vol. 10, no. 12, pp. 11304-11316, 2016/12/27 2016, doi: 10.1021/acsnano.6b06466.

[113] D. Stoddart, A. J. Heron, E. Mikhailova, G. Maglia, and H. Bayley, "Single-nucleotide discrimination in immobilized DNA oligonucleotides with a biological nanopore," (in eng), *Proc Natl Acad Sci U S A,* vol. 106, no. 19, pp. 7702-7, May 12 2009, doi: 10.1073/pnas.0901054106.

[114] C. Wang, S. Sensale, Z. Pan, S. Senapati, and H. C. Chang, "Slowing down DNA translocation through solid-state nanopores by edge-field leakage," (in eng), *Nat Commun,* vol. 12, no. 1, p. 140, Jan 8 2021, doi: 10.1038/s41467-020-20409-4.

[115] J. A. Esteban, M. Salas, and L. Blanco, "Fidelity of phi 29 DNA polymerase. Comparison between protein-primed initiation and DNA polymerization," (in eng), *J Biol Chem,* vol. 268, no. 4, pp. 2719-26, Feb 5 1993.

[116] M. Wanunu, J. Sutin, B. McNally, A. Chow, and A. Meller, "DNA translocation governed by interactions with solid-state nanopores," (in eng), *Biophys J,* vol. 95, no. 10, pp. 4716-25, Nov 15 2008, doi: 10.1529/biophysj.108.140475.